Die approbierte Originalversion dieser Diplom-/Masterarbeit ist in der Hauptbibliothek der Technischen Universität Wien aufgestellt und zugänglich.
http://www.ub.tuwien.ac.at

The approved original version of this diploma or master thesis is available at the main library of the Vienna University of Technology.
http://www.ub.tuwien.ac.at/eng

TECHNISCHE UNIVERSITÄT WIEN
Vienna University of Technology

Diplomarbeit

Impact of different Spray Patterns on Mixture-Preparation and Pre-Ignition Tendency of a Direct-Injection Gasoline Engine

ausgeführt zum Zwecke der Erlangung des akademischen Grades einer Diplom-Ingenieurin unter der Leitung von

Dipl.-Ing. Michael Heiß

und

Associate Prof. Dipl.-Ing. Dr.techn. Thomas Lauer

E315
Institut für Fahrzeugantriebe und Automobiltechnik

eingereicht an der Technischen Universität Wien
Fakultät für Maschinenwesen und Betriebswissenschaften
von

Elisabeth Staudigl
0725696
Rathausstrasse 15
2253 Weikendorf

Wien, Jänner 2015

Diese Arbeit entstand auf dem Institut für Fahrzeugantriebe und Automobiltechnik der Technischen Universität Wien im Rahmen eines Projektes mit Jaguar Land Rover.

Seitens des Instituts möchte ich mich bei *Ass. Prof. Dipl. Ing. Dr. Thomas Lauer* für seine Unterstützung bedanken.

Für die umfassende fachliche Betreuung und hilfreichen Anregungen gebührt mein Dank *Dipl. Ing. Michael Heiß*.

Besonders bedanken möchte ich mich bei meiner Familie, insbesondere bei meinen Eltern, für die großartige und langjährige Unterstützung, weit über mein gesamtes Studium hinaus.

Danken möchte ich auch meinem Partner, sowie meinen Mitbewohnern und Freunden, für ihr Verständnis und vor allem für die großartige Unterstützung während der gesamten Entstehungsphase.

Eidesstattliche Erklärung

Ich habe zur Kenntnis genommen, dass ich zur Drucklegung meiner Arbeit unter der Bezeichnung

Impact of different Sprays Patterns on Mixture-Preparation and Pre-Ignition Tendency of a Direct Injection Gasoline Engine

nur mit Bewilligung der Prüfungskommission berechtigt bin. Ich erkläre weiters an Eides statt, dass ich meine Diplomarbeit nach den anerkannten Grundsätzen für wissenschafliche Arbeiten selbständig ausgeführt habe und alle verwendeten Hilfsmittel, insbesondere die zugrunde gelegte Literatur genannt habe.

Weiters erkläre ich, dass ich dieses Diplomarbeitsthema bisher weder im In- noch im Ausland (einer Beurteilerin/ einem Beurteiler zur Begutachtung) in irgendeiner Form als Prüfungsarbeit vorgelegt habe und dass diese Arbeit mit der vom Begutachter beurteilten Arbeit übereinstimmt.

Wien, am 14.1.2015

Sperrvermerk:

Ich weise darauf hin, dass die Diplomarbeit vertrauliche Informationen und unternehmensinterne Daten beinhaltet. Daher ist eine Veröffentlichung oder Weitergabe von Inhalten an Dritte ohne die vorherige Einverständniserklärung des Instituts für Fahrzeugantriebe und Automobiltechnik nicht gestattet.

Contents

Nomenclature **v**

1 Introduction **1**

2 Scope of this thesis **3**

3 Theoretical Background **5**

3.1 Abnormal combustion 5
3.2 Spray Formation 10
3.3 Break-up Within the Atomization Regime 12
3.4 Multi Component Fuel 16
3.5 Multiphase Flow 18
3.6 Geometry Change during Runtime 28

4 Bomb Experiment Studies **30**

4.1 Injector Properties and Boundary Conditions 32
4.2 Investigated Break-up Models 34
4.3 Comparison between Primary and Secondary Break-up 37

5 Injection Processes Inside an Engine Model **44**

5.1 Mesh Generation and Model Set-up 44
5.2 Influence of Different Injector Types on the Charge Motion . . . 47
5.3 Influence of Different Injector Types on the Mixture Preparation 51

6 Summary and Conclusion **66**

Bibliography **71**

Nomenclature

Abbreviations

Re	Reynolds Number
Sh	Sherwood Number
We	Weber Number
Z	Ohnesorge Number

Symbols

A	surface area [m^2]
B	non-dimensional impact parameter [-]
c_p	specific heat capacity at constant pressure [$\mathrm{J\,kg^{-1}\,K^{-1}}$]
c_{am}	virtual mass coefficient [-]
c_D	drag coefficient [-]
C	constant [-]
d	droplet diameter [m]
D	diffusion coefficient [$\mathrm{m^2\,s^{-1}}$]
	drop diameter [m]
f	body forces [$\mathrm{N\,m^{-3}}$]
F	force [N]
	mass transfer rate per unit surface [$\mathrm{kg\,s^{-1}\,m^{-2}}$]
h	specific Enthalpy [$\mathrm{J\,kg^{-1}}$]
	latent heat of phase change [$\mathrm{J\,kg^{-1}}$]
	heat transfer coefficient [$\mathrm{W\,m^{-2}\,K^{-1}}$]
	mass transfer coefficient [$\mathrm{m\,s^{-1}}$]
k	specific turbulent kinetic energy [$\mathrm{J\,kg^{-1}}$]
	wave number [-]
K	mass transfer coefficient [$\mathrm{m\,s^{-1}}$]
L	characteristic length scale [m]

m	mass [kg]
p	pressure [Pa]
q	specific thermal energy [$\mathrm{J\,m^{-3}}$]
q''	surface heat flux [$\mathrm{W\,m^{-2}}$]
Q	heat transfer [J]
$\dot{Q}$	heat flux [W]
r	droplet radius [m]
R	gas constant [$\mathrm{J\,kg^{-1}\,K^{-1}}$]
t	time [s]
T	Temperature [K]
$\vec{u}$	vector of droplet velocity [$\mathrm{m\,s^{-1}}$]
$\vec{v}$	vector of gas velocity [$\mathrm{m\,s^{-1}}$]
u	velocity component in x-direction [$\mathrm{m\,s^{-1}}$];
	specific internal energy [$\mathrm{J\,kg^{-1}}$];
v	velocity component in y-direction [$\mathrm{m\,s^{-1}}$]
V_d	drop volume [$\mathrm{m^3}$]
w	velocity component in z-direction [$\mathrm{m\,s^{-1}}$]
$\vec{x}$	vector of droplet position [m]
y	droplet distortion parameter [-]
$\dot{y}$	oscillation velocity [$\mathrm{s^{-1}}$]
Y	specie mass fraction [-]

Greek Letters

α	circumferential spray angle [°]
β	spray cone angle [°]
ε	dissipation rate of turbulent kinetic energy [$\mathrm{m^2\,s^{-3}}$]
η	wave amplitude [m]
Φ	Liquid core angle [$\mathrm{rad^{-1}}$]
λ	air-fuel equivalence ratio [-]
	thermal conductivity [$\mathrm{W\,m^{-1}\,K^{-1}}$]
	wave length [m]
Λ	wave length of fastest growing wave [m]
μ	dynamic viscosity [$\mathrm{kg\,m^{-3}}$]
ρ	density [$\mathrm{kg\,m^{-3}}$]
σ	surface tension at the liquid-gas interface [$\mathrm{N\,m^{-1}}$]
τ	stress tensor [$\mathrm{N\,m^{-2}}$]
	characteristic time scale [s]
ω	growth rate [$\mathrm{s^{-1}}$]
Ω	growth rate of most unstable wave [$\mathrm{s^{-1}}$]

Subscripts

b	general body
c	critical state
d	droplet
dr	drag
g	gas phase
i, j	variable index, Einstein notation
l	liquid phase
m	variable index
s	surface

Kurzfassung

Gegenwärtig werden Downsizing Strategien in der Motorenentwicklung verfolgt, um ökologischen Standards bei gesteigertem Wirkungsgrad nachzukommen. Jedoch limitieren Verbrennungsanomalien die weitere Effizienzsteigerung, da bei hohen Lasten und moderaten Drehzahlen Vorentflammungen eine stark klopfende Verbrennung verursachen. Forschungsarbeiten zu diesem Phänomen konnten abgelöste Öl-Kraftstoff Tropfen, welche die Zündwilligkeit des Gemisches erhöhen, als wahrscheinlichste Ursache für Vorentflammungen identifizieren. Die Vermischung von Öl und Kraftstoff in Wandfilmansammlungen stellt somit das Hauptproblem dar.

Im Zuge dieser Arbeit werden mittels numerischer Simulation diese Wandfilmansammlungen an einem direkteinspritzenden Ottomotor im Detail untersucht. Da der Einspritzvorgang großen Einfluss auf die Gemischbildung hat, wird der Tropfenzerfall mittels Primär und Sekundäraufbruchsmodelle untersucht. Dabei wird besonderes Augenmerk auf die Validierung der Tropfenaufbruchmodelle gegen Meßdaten gelegt. Das korrekte Siedeverhalten von Benzin wird mit einem Mehrkomponenten Kraftstoffmodell abgebildet, welches in der Lage ist schwerflüchtige Komponenten zu berücksichtigen. Anhand eines Vergleichs zweier Injektortypen wird der Einspritzvorgang, sowie die Wandfilmformationen auf die potentielle Vermischung mit Öl hin verglichen. Flüssigfilm Ansammelungen insbesondere an den Zylinderwänden und im Kolbenspalt werden für jede Injektorausführung identifiziert.

Die Untersuchungen zu den Auswirkungen auf Gemischbildung und Ladungsbewegung zeigen, dass steil in den Zylinder weisende Injektorachsen vorteilhaft sind. Es verbessert sich sowohl die Gemischbildung und es minimiert sich die Vermischung mit Öl. Es zeigt sich, dass der mittels Simulation erhaltene Wandfilm mit entsprechenden Beobachtungen auf dem Prüfstand korreliert. Die gewonnen Faktoren leisten einen Beitrag zum besseren Verständnis und daher zur Vermeidung von Vorentflammung.

Abstract

Recent developments in engine production focus on downsizing strategies in order to meet ecological restrictions while improving efficiency. However, abnormal combustion phenomena limit further improvements since premature ignitions, which occur at higher engine torque and lower engine speed, initiate severe knock in the subsequent combustion. In order to get to the root of the problem, investigations on this topic revealed that lubrication oil mixed with fuel increases auto-ignition of the mixture and hence causes pre-ignitions, if oil-fuel mixture droplets enter the combustion chamber and heat up. Therefore, the main problem is that mixing of lubrication oil and fuel can take place in liquid film accumulations.

Within this thesis, the pre-ignition tendency of a direct injection gasoline engine is explored and investigated in detail conducting numerical simulations. Since the injection process has proven to have a huge impact on mixture preparation, droplet disintegration models for primary and secondary break-up are investigated with special attention for the validation of the numerical injection set-up against measurement data. A multicomponent fuel model is applied in order to represent the boiling behaviour of real gasoline as realistic as possible. By comparing two different injector types, the injection process and wall-film formations are investigated with regard to possible mixing of fuel and oil. Liquid film accumulations at the cylinder walls and in the piston crevice are identified and investigated for each injector type.

Detailed investigations on mixture preparation and charge motion revealed that steep into the cylinder orientated injector axes are advantageous. Improvements in mixture preparation and a minimised mixing with oil is observed. Results show that the numerical prediction of wall-film structure can be correlated to test-bench observations. Therefore, the gained factors contribute to a better understanding and hence to avoid pre-ignitions.

1 Introduction

Increasing standards on efficiency and fuel consumption in engine development forces engineers to exhaust the limits of thermodynamic possibilities. Nowadays, downsizing strategies are pursued for gasoline engines to fulfil ecological and political standards and requirements, which are depicted in Figure 1.1.

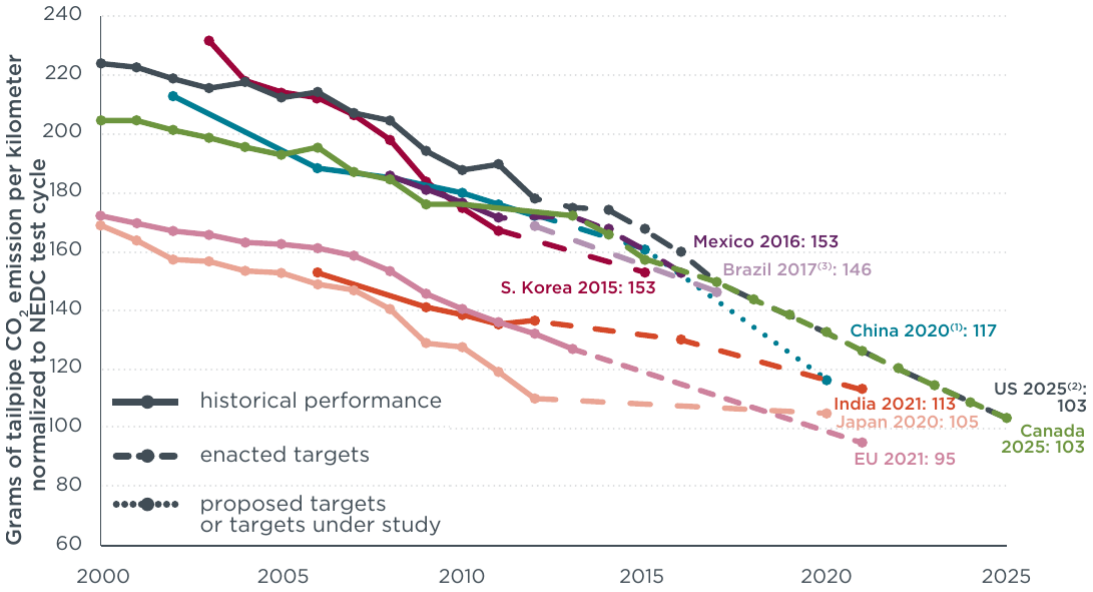

[1] China's target reflects gasoline vehicles only. The target may be higher after new energy vehicles are considered.
[2] US fuel economy stadards set by NHTSA reflecting tailpipe GHG emission (i.e. exclude low-GWP refrigerant credits).
[3] Gasoline in Brazil contains 22% of ethanol (E22), all data in the chart have been converted to gasoline (E00) equivalent.
[4] Supporting data can be found at: http://www.theicct.org/info-tools/global-passenger-vehicle-standards

Figure 1.1: Comparison of global CO_2 regulations for new passenger cars, reprinted from ICCT [1].

By reducing the engine displacement, improved fuel efficiency in part-load operation can be achieved. The nominal power in full load operation is maintained by charging, which leads to higher torque at lower engine speed. This happens at the expense of combustion stability, which in turn increases emissions or even worse, leads to abnormal combustion mechanisms. Under these circumstances, high pressure levels but low engine speed, pre-ignitions and particularly Low Speed Premature Ignition (LSPI) take place. These can lead to serious damage

or destruction of the engine. As these phenomena are the limiting factors in engine development, a lot of effort is taken in order to prevent their occurrence. Modern engines are equipped with knock sensors that interact with the engine control system, preventing its repetition. Therefore, engine knock can be avoided at the cost of efficiency, however in combination with LSPI, anti-knock measures have proven to be ineffective.

In recent years, a lot of attention has been paid to LSPI and thus has become a frequent topic in research. A multitude of possible causes have been proposed and different mechanisms were investigated, conducting both test-bench observations as well as numerical methods. More details on these investigations can be seen e.g. Zahdeh et al. [2] and Dahnz et al. [3]. The authors agreed that the mixture of lubrication oil and fuel might initiate these kind of pre-ignition. Mixing takes place in liquid film accumulations at the liner walls and within the piston crevice. The surface tension of this mixture is lowered and therefore, droplets might strip off these accumulations and heat up, which can finally cause a pre-ignition.

Dependent on each individual engine constellation, different mechanisms might become dominant. Therefore, computational fluid dynamic *CFD* is adopted in order to identify these various influences and to asses their probability to become important. Numerical simulations allow deeper insights into the particular circumstances inside the engine where measurements are impossible.

Besides the thermodynamics, especially spray targeting, droplet impingement and wall-film structures at the piston and the liner are investigated within the CFD framework. By imitation of real gasoline, a multicomponent fuel with high boiling temperature components is introduced, since it has been shown in Heiß et al. [4], that a single component fuel differs significantly in wall-film prediction. It will be shown that different spray patterns have a huge impact on both, charge motion as well as mixture preparation. Therefore, investigating the impact of each spray pattern can provide important information on the detailed phenomena and mechanisms causing LSPI.

2 Scope of this thesis

Gasoline engines incorporate turbo-charging and direct injection technologies in order to meet future ecological standards of CO_2 emissions. However, especially in full load operation at low engine speed, an increase in efficiency is limited by spontaneous auto-ignition of the charge before the onset of regular spark timing. The subsequent knocking combustion can lead to engine breakdown within a few pre-ignited cycles. A possible explanation for these auto-ignition events is the mixing of injected fuel with lubrication oil in areas near the piston crevice and the cylinder liner. The spray geometry with its corresponding spray pattern, as well as the deflection of the spray due to the intake flow might cause extended liquid film formation at the combustion chamber walls. Oil-fuel mixture droplets have proven to lower auto-ignition delay times and might cause premature ignitions if a drop is stripping off the liquid film structures. Within the framework of this thesis, the impact of different spray patterns on mixture preparation and wall-film formation should be determined with the objective to gain additional information on the pre-ignition tendency.
The scope of this thesis involves:

1. literature review
2. investigations, using CFD-simulations, with the software tool *STAR-CD*
   - creation and application of a static CFD model, for the verification of the numerical injection parameter against high speed imaging of the injection process
   - creation of a dynamic model of an engine (including piston and valve motion) with the software tool *es-ice*
   - implementation and application of different spray patterns, in order to determine the injection process and the mixture preparation process with the software tool *pro-STAR*

- comparison, assessment and interpretation of the simulation results with regard to:
  - wall-film formation
  - fuel vaporisation
  - mixture distribution
  - pre-ignition tendency

3 Theoretical Background

Internal combustion engines are fascinating people already for more than a hundred years. Since then, a lot of research has been conducted in order to get deep insights into the exact functioning. Nowadays, numerical methods accompanied with test bench measurements are the chosen tools to develop engines with higher efficiency while reducing emissions.
The aim of the next chapter is to explore the limiting mechanisms in current engine development. Subsequently, a deeper understanding on the different processes, which are numerically modelled and optimized for the application in a combustion engine simulation, is provided.

3.1 Abnormal combustion

Abnormal combustion phenomena, such as knock, surface ignition, and pre-ignition, limit current engine downsizing developments.
In general, abnormal combustion is caused by auto-ignition of the charge. Knock is usually referred to as the auto-ignition of the end-gas ahead of the propagating flame during power stroke. Premature ignition in contrast, occurs before the onset of regular spark discharge. This advance in spark timing can cause severe knock with extreme high pressure amplitudes, see Dahnz et al.[3]. Measures to prevent one abnormal combustion phenomena in turn can have an impact on the occurrence of other ones, e.g. a reduction of the spark advance for preventing knock can cause pre-ignitions, see Yasueda [5]. Moreover, it has been shown, that one phenomenon can trigger another one. According to Dahnz et al. [3], a pressure wave due to knock can interfere with the surface boundary layer and hence elevate the heat transfer. Hot walls can then initiate surface ignition in the next cycle.
In order to prevent abnormal combustion, a clear differentiation between the phenomena and the factors which initiate them is of great importance.

3.1.1 Engine knock

'Knock' is perceptible by the sound transmitted through the engine structure when pressure waves excite the neighbouring components.
After regular spark timing, some regions within the end-gas reach the auto-ignition point earlier than others, dependent on their local thermodynamic states. Auto-igniting pockets within the unburned mixture suddenly explode, releasing pressure waves. Those shock waves are reflected at the combustion chamber walls, creating high frequent oscillations of the pressure, which excite the eigenmodes of the combustion chamber structure. A typical pressure trace of a knocking combustion is depicted in Figure 3.1. One can see that pressure peaks become considerably higher than in regular combustion, putting a high load on the engine structure.

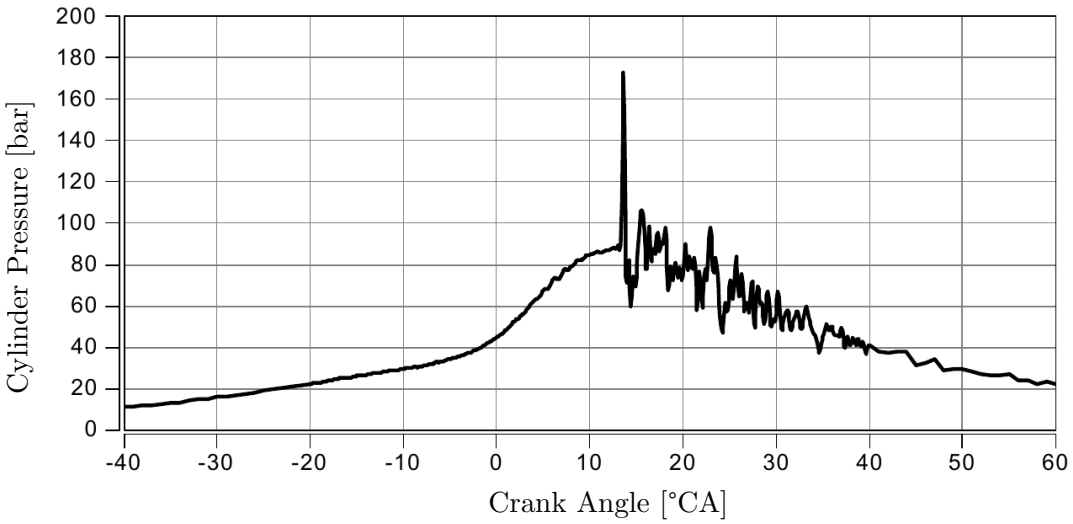

Figure 3.1: Pressure trace for knocking combustion, reprinted from Merker [6] p.149.

However, knock is a process which can only take place if enough time and the corresponding thermodynamic states for auto-ignition are available. Therefore, knock controls retard spark timing in order to decrease pressure and temperature gradients, see Merker [7]. However, this process decreases efficiency, therefore, if regular combustion takes place again, ignition timing is step wise reset in order to operate with the highest possible efficiency, see Basshuysen [8] pp.87.

3.1.2 Pre-Ignitions

Premature ignition is the generic term for all types of ignitions, which occur before the onset of regular spark timing. The characteristic pressure trace of

a pre-ignited cycle, in comparison to a regular cycle (dashed line) is shown in Figure 3.2. One can see, that the peak pressure occurs a little bit earlier than in the normal cycle. Additionally, also the peak pressure level is raised, amplitudes double the size of the regular pressure level develop already before the onset of regular spark timing.

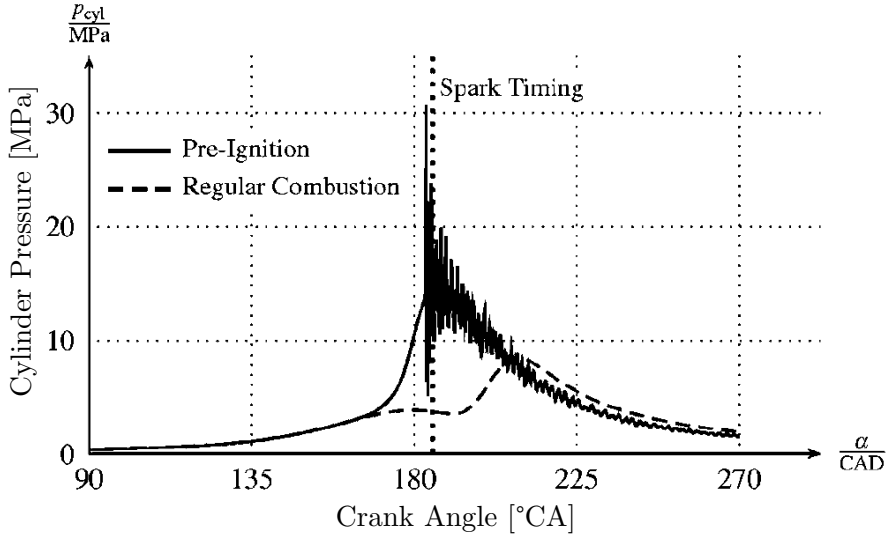

Figure 3.2: Pressure trace for pre-ignition, reprinted from Dahnz et al. [3].

The advance in ignition timing forces the engine to compress an expanding gas, which releases additional heat during compression. This puts not only enormous loads onto the engine, but also increases the temperature of the parts. Generally, pre-ignitions lead to a raised pressure level, which can initiate a knocking combustion in a second stage with pressure spikes as depicted in Figure 3.2.
Engine damage or breakdown is the result, dependent on the stochastic frequency of pre-ignitions and the severity of subsequent knock. According to Yasueda [5], a strict differentiation between cause and effect allows to classify pre-ignition events as belonging to different groups. These are now discussed in more detail.

In Figure 3.3 an overview of probable mechanisms, highlighting also their probability of initiating low speed premature ignition (LSPI), is provided.

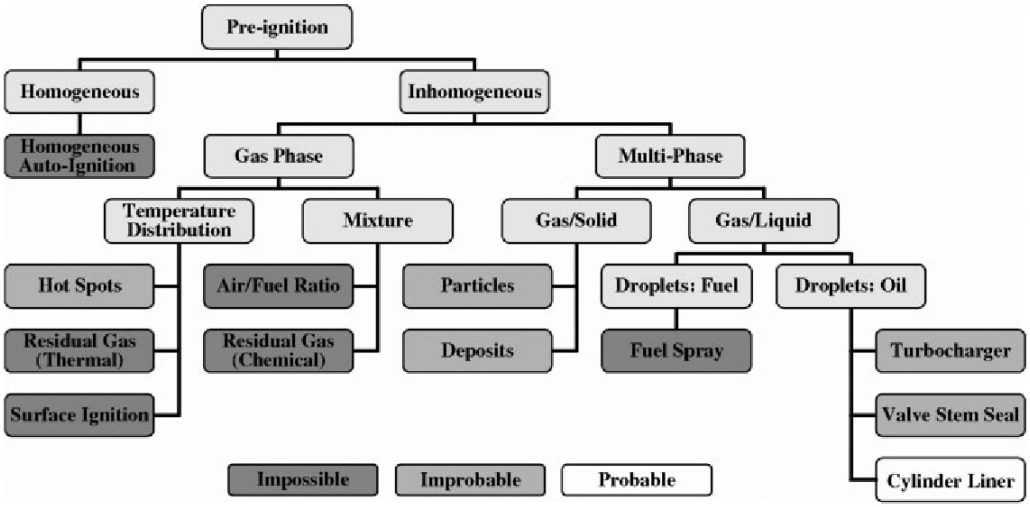

Figure 3.3: Overview of different pre-ignition mechanisms, Figure reprinted from Dahnz et al. [3].

Surface Ignition

In surface ignition the mixture is auto-ignited by a hot surface within the combustion chamber. This typically results in engine knock, and since this amplifies heat transfer, auto-ignition occurs earlier in the next cycle, causing even stronger knock. As auto-ignition timing is constantly moving forward up to intake valve closing, a self-preserving or self amplifying process establishes. Engine breakdown occurs unstoppable within a view cycles, see Dahnz et al. [3]. However, Dahnz et al. [3] ruled surface ignition as possible cause for pre-ignitions out, see Figure 3.3. Nevertheless, hot surfaces have to be avoided in order to prevent engine breakdown. A possible way to do this is by an appropriate dimensioning of the cooling system, by improvement of the spark plug material and orientation and by avoiding any sharp edges within the combustion chamber, see Dahnz et al. [3] and Zahdeh et al. [2] .

Hot Objects Within the Combustion Chamber

Other reported causes for pre-ignitions are hot objects within the combustion chamber. These objects might be hot particles not rinsed out, or other possible objects, such as hot residual gas, or mixture inhomogeneities, see Merker [7] and Dahnz et al.[9]. In contrast to surface ignition, these auto-ignition events occur stochastically only once, followed by a regular combustion. This type of pre-ignition occurs during intake stroke or early in compression stroke, see

Yasueda [5]. Consequently, peak pressure increases and correspondingly also the gas temperature. Therefore, knock might be initiated in the subsequent expansion stroke. Engine breakdown does not occur as fast as in surface ignition, but as severity increases, breakdown is only a matter of time. Even though it is theoretically possible that one of these mechanisms might cause LSPI, extended investigations in Dahnz et al.[9] revealed, that also another source causing LSPI must exist, compare with Figure 3.3.

Engine Oil caused Auto-Ignition

As Figure 3.3 presents, Dahnz et al.[3] determined oil droplets, stripping off the cylinder liner, as the most probable mechanism causing pre-ignitions.
Low speed pre-ignitions (LSPI) is a stochastic phenomenon, which temporally occurs just before spark plug discharge (according to Yasueda [5] 5-15 °CA up to 20 °CA reported in Heiß et al. [10]). It mostly occurs in intermittent sequences, and after some cycles regular combustion returns, see Dahnz [3]. According to Yasueda [5], LSPI happens more often, with ongoing time, and severity increases with rising frequency. However, this type of pre-ignition tends to cause severe knock, which leads to piston or connecting rod damage. Moreover, engine breakdowns within one cycle were observed, see Zaccardi et al. [11].
In past years, lubrication oil has been determined to cause this type of pre-ignitions, see Palaveev et al. [12] and Zahdeh et al. [2]. As it turns out, lubrication oil mixing with fuel lowers the auto-igniting temperature of the mixture. This might cause pre-ignition if oil-fuel mixture droplets enter the combustion chamber and heat up. Additionally, the presence of oil in liquid fuel accumulations lowers the surface tension. Therefore, drop stripping might occur more easily. It has been observed, that pre-ignitions are initiated remotely from surfaces. Therefore, oil droplets, or oil-fuel mixture droplets have to be released. These drops strip off a liquid film, positioned at any combustion chamber surface. A possible mechanism, showing how oil droplets are released from the piston crevice area, is depicted in Figure 3.4.

The influence of different base oil and additives seems to have great influence on LSPI, see Takeuchi et al. [13]. Also measurements, which improve mixture preparation have a decreasing effect on the pre-ignition frequency. Due to

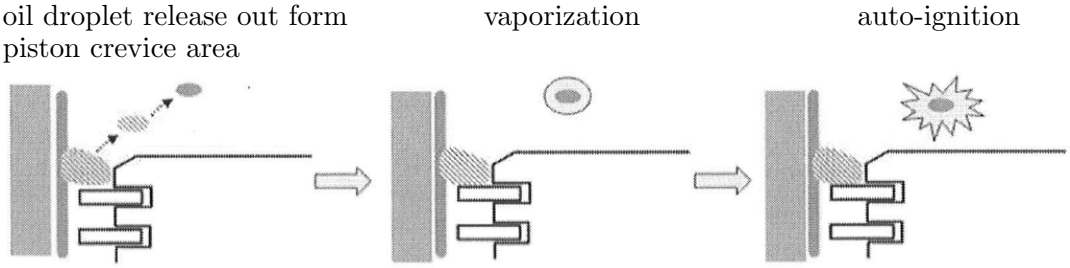

Figure 3.4: Auto-ignition cause by an oil drop from the piston crevice, reprinted from Takeuchi [13].

improved vaporisation, less liquid fuel can mix with oil, see Zahdeh et al. [2] and Yasueda [5]. Especially the injection process and wall-film formations at the cylinder liner have turned out to be an important factor causing pre-ignitions. A detailed investigation on that topic is provided in Heiß et al. [10]. Their detailed investigations revealed possible drop traces released from film accumulations within the piston crevice, and compared them to pre-ignition initiation.
Therefore, a possible way to avoid LSPI is by avoiding liquid film accumulations, which allow droplet stripping. Hence, the following points proposed by Zahdeh et al. [2] and Danhz et al. [3] should be avoided :

- spray targeting on the cylinder liner
- spray striking surfaces and stripping lubrication oil
- stripping of oil/oil-fuel droplets from wall-film due to gas motion
- ejection of oil/oil-fuel droplets due to piston acceleration
- oil-fuel mixture evaporating from the cylinder liner/piston

3.2 Spray Formation

As spray formation is influencing the pre-ignition tendency in multiple ways, modelling its correct functionality is crucial in order to predict mixing accurately. At first, the characteristics of spray propagation are introduced, in order to understand the difficulties in modelling a spray. Influencing effects are reviewed and the dominating processes, used to model these phenomena, are introduced.

Figure 3.5 shows the evolution of a high pressure injection spray. At the exit of the nozzle there has to be a substantial pressure difference in order to gain high injection velocities, which ensure a prompt breakup and evaporation of the liquid fluid. The fluid entering the domain displaces and entrains the surrounding gas and the two phases mix with each other. At the nozzle exit a liquid core is built. As it penetrates further into the domain, droplets and ligaments at the size of the nozzle diameter disintegrate. The counteraction of the gas phase induces surface waves on the liquid core, which can amplify at its surface forcing the liquid to release tiny droplets. Therefore, fuel vapour consisting of tiny droplets at the size of about 10 µm are enveloping the spray, see Heywood [14].

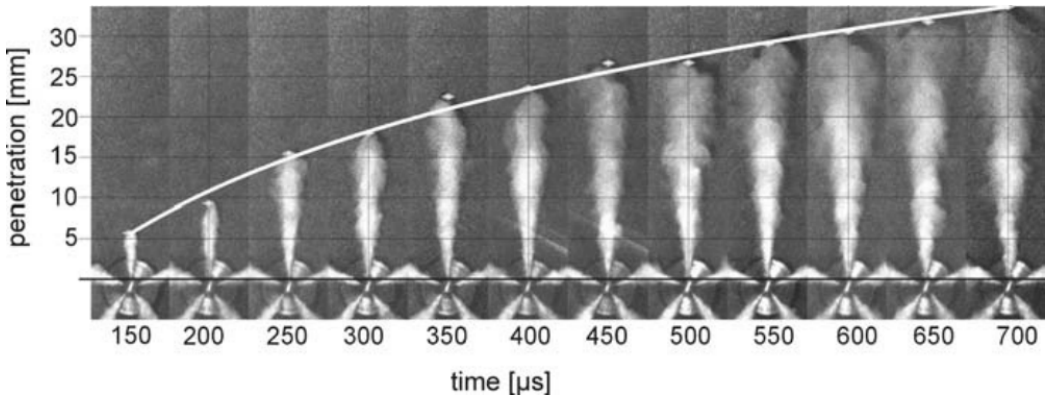

Figure 3.5: Development and evolution of a liquid spray during time at Δp =65 MPa. Reprinted from Baumgarten [15]pp.11.

The outer region of the cross-section interacts directly with the surrounding gas, and the spray diverges due to turbulence as one moves further downstream, forming a conical spray (spray cone angle Φ). Due to turbulence and different flow structures within the jet, gas is transported toward the inner regions of the spray. This increases the existing gas mass fraction, and fuel droplets continue evaporating.

In the meantime the droplets at the tip of the spray experience massive deceleration due to aerodynamic forces. The foremost droplet breaks up and the residuals are pushed aside while other droplets pass constantly, which then experience the same. The length between the nozzle exit and the first breakup of the core is called '*break-up length*', and describes the characteristic length scale of a spray.

3.2.1 Spray Classification

In order to describe the occurrence of the mechanisms mentioned above, the flow conditions are classified according to their position inside the spray, their relative velocity and the fluid properties using the well known Reynolds and Weber number. Combining them leads to the Ohnesorge number Z:

$$Re_l = \frac{\rho_l u_l L}{\mu_l} \qquad We_l = \frac{\rho_l u_l^2 L}{\sigma} \qquad Z = \frac{\sqrt{We}}{Re} = \frac{\mu}{\sqrt{\rho \sigma L}} \tag{3.1}$$

l denotes the liquid phase, L is a characteristic length, u the jet velocity, ρ the correspondent density, μ the dynamic viscosity and σ the surface tension at the liquid-gas interface. The *Reynolds* number represents the ratio of the inertia to viscous forces, whereas the Weber number is composed of the ratio between inertia forces and surface tension forces. Combining them to Z eliminates the velocity dependence and results in a representative fluid property number. Dependent on these fluid properties one can classify several spray regimes.

In engine applications, high injection pressures and small nozzle hole diameter cause an immediate break-up of the injected fuel into small droplets and ligaments direct at the nozzle exit, which is called atomization. However, a more or less intact liquid core consisting of liquid filaments may still be existent.

3.3 Break-up Within the Atomization Regime

Within the atomization regime, at first liquid ligaments and drops will form at the size of the nozzle diameter developing a liquid (or dense) core, shown in Figure 3.6. The characteristics of this liquid core are strongly influenced by the flow conditions inside the nozzle. Cavitation, hydrodynamic instabilities, turbulence and processes due to the change in the velocity profile dominate the formation of the liquid core. Primary break-up is the collective term for these mechanisms in summary.
Secondary break-up is the process where the already formed droplets and ligaments disintegrate again in a multitude of tiny droplets, which is caused by aerodynamic forces, shown in the middle section of Figure 3.6.

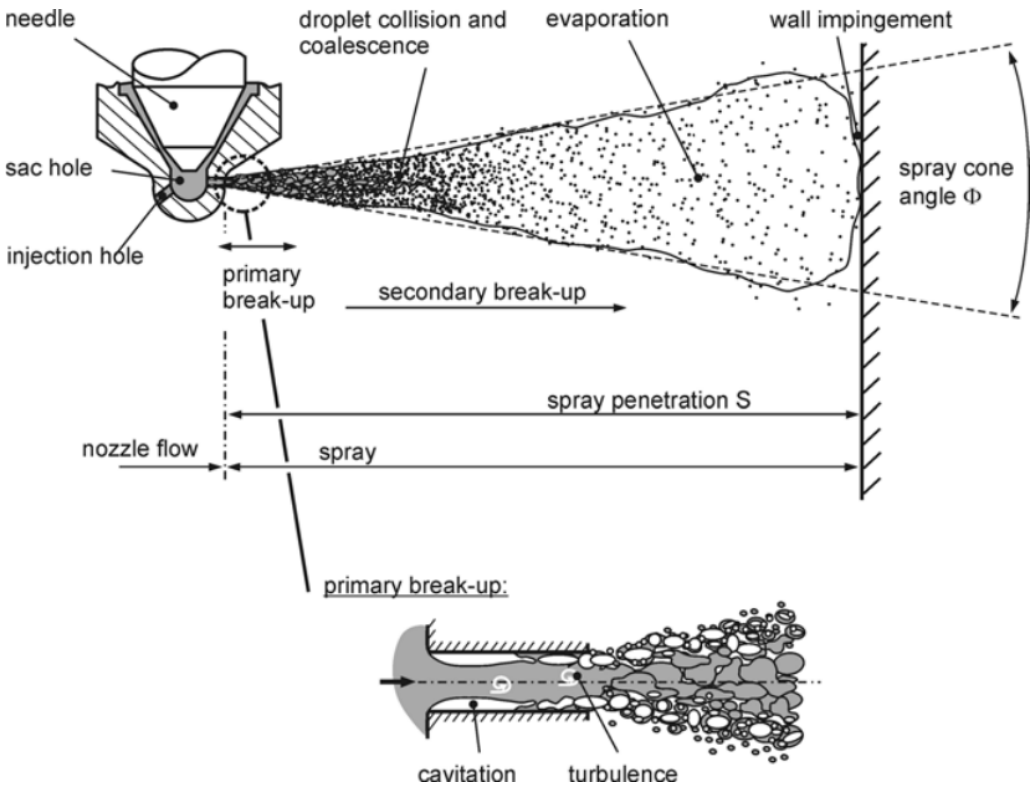

Figure 3.6: Engine spray disintegration processes, reprinted from Baumgarten [15] pp.10.

3.3.1 Secondary Break-up Mechanisms

Secondary break-up is classified according to different initiating mechanisms. The disruptive aerodynamic force and the restorative surface tension force have a crucial role in drop break-up. Their ratio is given by the Weber number in equation (3.1). The larger the Weber number, the larger is the tendency of the drop toward break-up. Viscosity plays the counterpart of this tendency, it hinders the deformation and dissipates the energy supplied by aerodynamic forces.

A classification according to the local Weber number is used to distinguish between the different break-up modes and mechanisms, see Figure 3.7. Transition between these regimes is a continuous function of Weber numbers and also several mechanisms may interfere with each other.

Details on the different processes, which lead to the single break-up mechanisms are provided in Ashgriz [16].

In general, these break-up mechanisms apply to all engine sprays and no distinction between the fuel type is necessary.

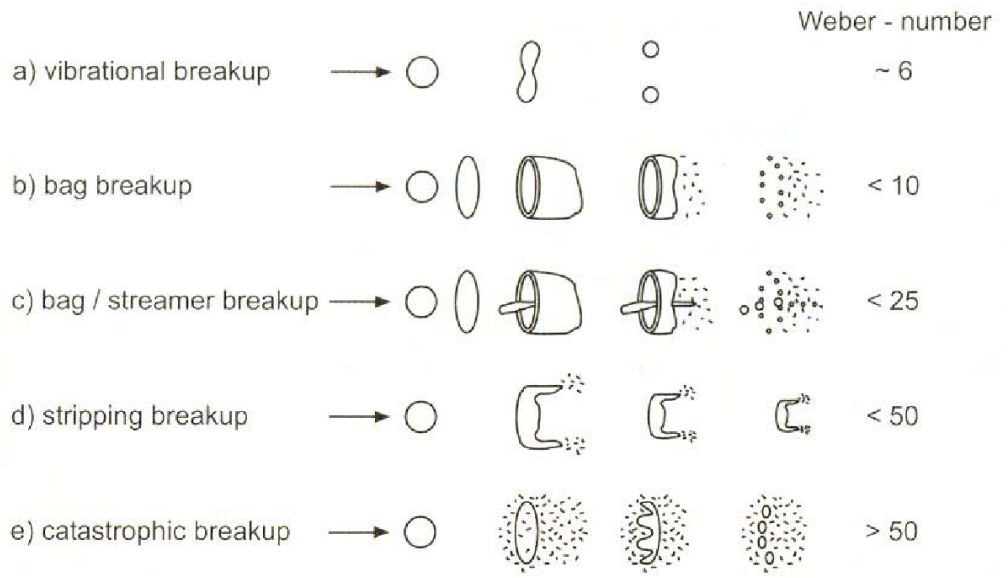

Figure 3.7: Different secondary atomization mechanisms of individual drops, reprinted from Wierzba [17].

However, in gasoline engines break-up occurs at lower Weber number regimes, because of the lower injection pressure. Figure 3.8 presents the relevant secondary break-up regimes for different engine applications.

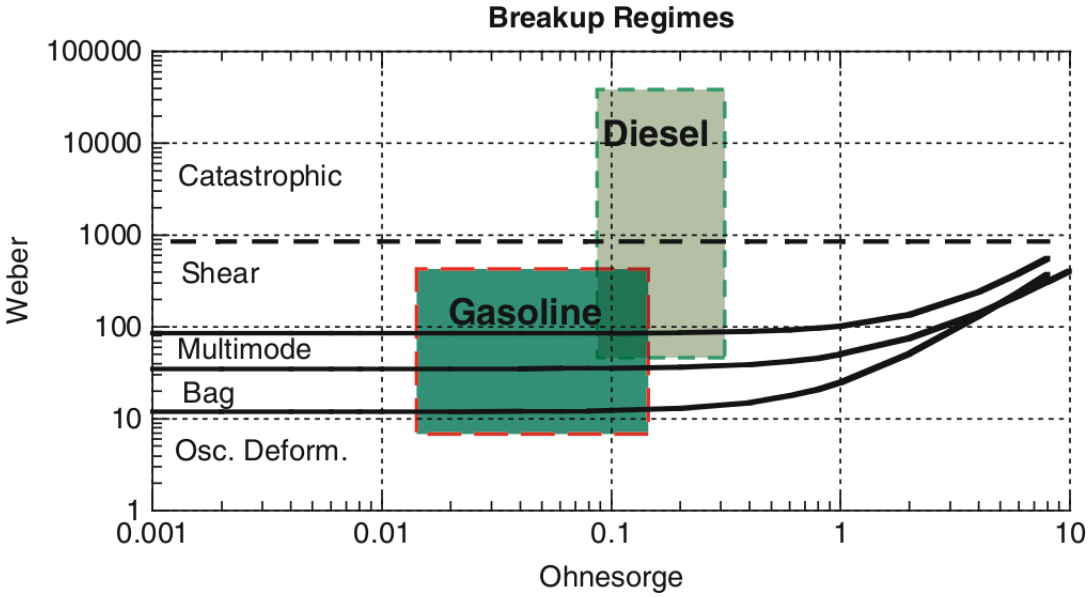

Figure 3.8: Secondary break-up regimes with highlighted diesel and gasoline fuel regimes, Weber number relates the injection velocity, whereas *Ohnesorge* number represents fuel properties. Reprinted from Ashgriz [16]pp.225.

3.3.2 Break-up Models

Most atomization and break-up models are based on a stability analysis of a round jet or drop respectively, which is penetrating into a stationary incompressible gas environment. These theoretical relations, in combination with experimental observations, are used to model relations for *Primary* as well as for *Secondary Break-up*. Within this thesis, the following models are applied.

Primary Break-up Model

Huh's Model is based on the instability analysis of initial perturbations initiated by turbulence. It considers infinitesimal perturbations on the jet surface, which are generated as the turbulent jet exits the nozzle hole. Therefore, it can also predict cavitation dynamics. The basic correlations are presented in Table 3.1. Initial perturbations (surface waves) grow exponentially due to pressure forces acting due to interaction with the surrounding gas. If they have reached a certain level, these waves cause a detachment of droplets. This model assumes that the turbulence length scale is the dominant length scale for atomization. The atomization time scale is described as a linear combination of wave growth[1)] and turbulence time scale. On that basis, it determines the diameter distribution of secondary droplets and the spray semi-cone angle β.

Secondary Break-up Model

Reitz-Diwakar Model secondary break-up model is applied in the course of this thesis. It is based on an immediate disintegration, if a specific break-up condition is met. The model distinguishes between *Bag break-up*, due to a non uniform pressure field around the drop, and *Stripping break-up*, where the leading break-up mechanism is due to shear forces arising from relative velocities. The transition between those mechanisms is defined according to the Weber number:

$$\text{Bag break-up:} \qquad \mathrm{We} > 6$$

$$\text{Stripping breakup:} \qquad \frac{We}{\sqrt{Re}} > 0{,}5$$

[1)] STAR-CD introduced an exponential model constant, whereas in literature [16] parabolic correlations were considered

Table 3.1: Model for *Primary break-up* and *Secondary break-up*, details on the model variables are given in the Methodology [18].

	Huh	Reitz-Diwakar
Mode	Multimode Instability	Multimode Instability
Interaction Mechanism	linear combination of the dominant time scales	Regimes separated by Weber number
Break-Up Rate	$\frac{dD_d}{dt} = \frac{-2L_A}{(\tau_A \times 0,1)}$	$\frac{dD_d}{dt} = -\frac{(D_d - D_{d,sta})}{\tau_b}$
Effective timescale	$\tau_A = C_3\tau_t + C_4\tau_W$	Weber Number
Timescale 1	turbulent scale τ_t	Bag Break-up $\tau_b = \frac{C_{b_2}\rho^{\frac{1}{2}}D_d^{\frac{3}{2}}}{4\sigma_d^{\frac{1}{2}}}$
Timescale 2	surface wave growth τ_w	Strip Break-up $\tau_b = \frac{C_{s_2}}{2}\left(\frac{\rho_d}{\rho}\right)^{\frac{1}{2}}\frac{D_d}{u_{rel}}$

3.4 Multi Component Fuel

Gasoline is composed of a multitude of different components with different boiling temperatures. Dependent on the boiling temperature of each single component, its concentrations within the liquid phase vary, see Figure 3.9. Therefore, also the vapour pressure of a system consisting of multiple components varies dependent on the local concentrations.

Because of computational power reasons, it is a common approach in CFD simulations to consider the single component fuel n-Heptane as an alternative to gasoline. This is a valid approach, if details in wall-film formation and mixture inhomogeneities are not important. However, as the pre-ignition tendency is closely linked to these mechanisms, a single component fuel produces too crude results, see Heiß et al. [4], which is why a multicomponent fuel has to be considered. Batteh [19] presented a multicomponent fuel model which promises great improvements for a more accurate description of the details in mixture preparation and wall-film formation.

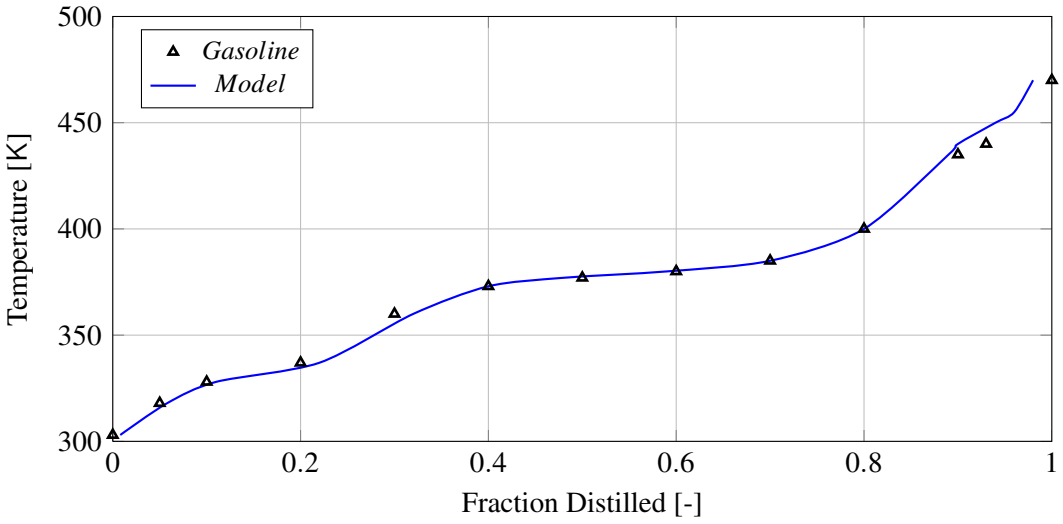

Figure 3.9: Boiling Curve, reprinted from Batteh [19].

Figure 3.9 compares the boiling behaviour of gasoline to a multicomponent fuel model. This fuel model consists of seven individual components, which are shown in Table 3.2. The model uses separate values for density, viscosity, surface tension and heat conduction coefficients of each component. Thermophysical

Table 3.2: Ingredients of the 7-component fuel, taken from Batteh [19], from top to bottom: component, chemical abbreviation, boiling temperature [K] and mass fraction.

n-Butane	Iso-pentane	n-Hexan	Isooctane	Toluol	1,2,3 Tri-methylbenzol	Tridekan
(C4H10)	(C5H12)	(C6H14)	(C8H18)	(C7H8)	(C9H12)	(C13H28)
272.3 K	300.7 K	341.6 K	372.0 K	383.4 K	448.8 K	507.9 K
4.00%	16.00%	2.50%	32.00%	25.50%	18.00%	2.00%

properties of each species, and the mixture properties (specific heat capacity, enthalpy of vaporisation, heat conductivity and its vapour pressure) are determined during runtime as a function of time. Individual vapour pressure curves of each component are defined in the dropro.f user subroutine as a function of time and temperature following the law of "Clausius-Clapeyron". More details on the implementation can be found in Waba [20].

3.5 Multiphase Flow

The gas phase within the combustion chamber consists of several constantly changing components (e.g. nitrogen, oxygen, fuel vapour). During injection, a second (liquid) phase also consisting of several components is present. Therefore, a short summary on modelling multiphase flows, which also allow spray and combustion processes, is provided in the following section.

3.5.1 Continuous Gas Phase

In multiphase flow systems, conservation equations for each single component within the continua need to be solved. Additional transport equations have to be solved, which take into account the change of each species concentration and chemical reactions. If additional phenomena, like evaporation, aerodynamic forces or heat exchange between the phases are of importance, additional mass, momentum and energy needs to be exchanged and therefore, auxiliary terms have to be added. These exchange terms are introduced by the *spray* and the *comb* term respectively. According to Amsden et.al [21], the continuity equation for each species m follows to:

$$\frac{\partial \rho_m}{\partial t} + \frac{\partial (\rho_m v_i)}{\partial x_i} = \frac{\partial}{\partial x_i}\left(\rho D \frac{\partial (\rho_m/\rho)}{\partial x_i}\right) + \dot{\rho}_{m,spray} + \dot{\rho}_{m,comb} \tag{3.2}$$

Here ρ_m specifies each specie's density and ρ the collective liquid density. v is the velocity in i direction following Einstein notation. The first term on the right hand side accounts for the specie's mass diffusion, with the diffusion coefficient D. The last two terms emerge due to spray and combustion respectively. Nevertheless, the continuity equation of the overall system has to be applied too, in order to ensure physical behaviour.

$$\frac{\partial \rho}{\partial t} + \frac{\partial (\rho v_i)}{\partial x_i} = \dot{\rho}_{spray} \tag{3.3}$$

This equation is composed of the sum over all single species m, which is required to be equal to the collective liquid density injected. The overall combustion term disappears, since chemical reactions do not change the total mass.
In the gas phase momentum equation, the liquid spray is accounted for by an additional source term $f_{j,spray}$. This term corresponds to the forces which act

on the gas phase due to the presence of a liquid spray:

$$\frac{\partial(\rho v_j)}{\partial t} + \frac{\partial(\rho v_j v_i)}{\partial x_i} = -\frac{\partial p}{\partial x_j} + \frac{\partial \tau_{ij}}{\partial x_i} + f_j + f_{j,spray} \tag{3.4}$$

With i, j following Einstein notation, τ_{ij} defines the stress tensor and f_j includes body forces e.g. gravitational force. Similar to the mass conservation equation an additional diffusion term appears in the energy equation (second term on the left hand side):

$$\rho\left(\frac{\partial}{\partial t} + u_j\frac{\partial}{\partial x_j}\right)u - \frac{\partial}{\partial x_j}\left(\lambda\frac{\partial T}{\partial x_i} + \rho D_m \sum_m h_m \frac{\partial(\rho_m/\rho)}{\partial x_i}\right) = -p\frac{\partial v_i}{\partial x_i} + \tau_{ij}\frac{\partial v_i}{\partial x_j} + q \tag{3.5}$$

More information and their derivation is given in Merker [7]. u corresponds to the internal energy and h to the specific enthalpy. The first term an the right hand side corresponds to the reversible mechanical work, while the second term takes additional heat due to internal friction into account. With the last term q, additional energy e.g. due to evaporation or combustion is regarded.
In order to determine the local composition of the gas field, additional transport equations (convection-diffusion equation) for the relevant scalar parameters (e.g. specie concentration) can be applied, see Merker [7].

Averaging the flow parameters according to the RANS approach enables the application in turbulent flows. Therefore, additional equations for the turbulent kinetic energy k and the dissipation rate ε have to be incorporated simultaneously. A great reference work for the derivations is given in Pope [22]. For the numerical implementation one is referenced to Ferziger and Peric [23].

3.5.2 Disperse Phase

A spray disintegrates into a multitude of droplets. Tracking all of them would exceed the computational possibilities. Following Williams [24], a phenomenological description of the spray can be modelled by introducing a statistical parameter, the probable number of droplets per unit volume or *droplet probability distribution function (PDF)* $f(\vec{x},\vec{u},r,T,t)$.

$$\frac{\textit{probable number of droplets}}{\textit{unit volume}} = f(\vec{x},\vec{u},r,T,t)d\vec{u}drdT \tag{3.6}$$

This function forms a problem of nine independent variables, which are time t, the droplet position $\vec{x}$ and velocity $\vec{u}$, its radius r and temperature T. With this knowledge, the temporal and spatial evolution of f can be written as a transport equation, the so called *spray equation*:

$$\frac{\partial f}{\partial t} = -\frac{\partial}{\partial x_i}(f u_i) - \frac{\partial}{\partial u_i}(f a_i) - \frac{\partial}{\partial r}(f\frac{dr}{dt}) - \frac{\partial}{\partial T}(f\frac{dT}{dt}) + \dot{f}_{bu} \tag{3.7}$$

Here a_i denotes the acceleration of the liquid drop in i direction per unit mass (Einstein summation). $\dot{f}_{bu}$ is a source term emerging due to droplet break-up and needs to be added into the conservation equations (mass, momentum and energy) of the gas phase, as discussed above.
In order to determine the rate of change of the distribution function f, groups of droplets, the so called '*parcels*', are considered. A *parcel* represents a group of identical drops with same properties which do not interact with each other. A collection of several *parcels* represents the droplet distribution in a spray spectrum. Position, velocity, size, density, and temperature of the parcels are determined by solving the basic conservation equations for the dispersed phase in *Lagrangian* description.

Lagrangian Equations

Mass and momentum equation in *lagrangian* description, given in the Methodology of the commercial software tool *STAR-CD* [18], with m_d the droplet mass and $\vec{u}_d$ its velocity, follows to:

$$\frac{dm_d}{dt} = -A_s F_m \tag{3.8}$$

$$m_d \frac{d\vec{u}_d}{dt} = \vec{F}_{dr} - V_d \nabla p - c_{am}\rho V_d \frac{d\vec{u}_{rel}}{dt} + \vec{F}_b \tag{3.9}$$

F_m is the mass transfer rate per unit surface and A_s the droplet surface and $\vec{F}_{dr}$ stands for the drag force given below. The second term on the right hand side accounts for the pressure force, and the third one is a so-called 'virtual mass', which models the gas acceleration entrained from droplets. V_d is the drop volume and p the pressure within the carrier fluid. $\vec{u}_{rel}$ is the relative velocity between drop and gas, and c_{am} the virtual mass coefficient. $\vec{F}_b$ represents general body forces by including the effect of gravity and pseudo forces arising in non-Cartesian coordinate systems.

The aerodynamic forces (drag forces) are modelled by considering a spherical drop, which has the radius r and moves relative to the gas with a velocity u_{rel}. This force correlates according to equation 3.10.

$$\vec{F}_{dr} = \frac{\rho_g}{2}\vec{u}_{rel}^2 c_D A_f = \rho_l \frac{4}{3}\pi r^3 \frac{d^2\vec{x}}{dt^2} \tag{3.10}$$

With c_D the drag coefficient and ρ_g the gas density. $A_f = \pi r^2$ represents the frontal area of the spherical drop and $\vec{x}$ is the coordinate along the droplet trajectory. For a perfect spherical drop, the drag coefficient is given accordingly to different Reynolds number regimes.

$$c_D = \frac{24}{Re_d}\left(1 + 0.15(Re_d^{0.687})\right) \qquad Re_d \leqslant 1000 \tag{3.11}$$

$$c_D = 0.44 \qquad Re_d > 1000 \tag{3.12}$$

The energy equation in Lagrangian description is:

$$m_d c_{p,d} \frac{dT_d}{dt} = -A_s \dot{q}_d'' + h_{fg} \frac{dm_d}{dt} \tag{3.13}$$

T_d is the droplet temperature, $c_{p,d}$ the droplets specific heat capacity, and h_{fg} the latent heat of phase change. $\dot{q}_d''$ is the surface heat flux, and $\frac{dm_d}{dt}$ is the mass transfer rate due to evaporation.

3.5.3 Multicomponent Droplet Evaporation

Evaporation is a process of diffusive and convective mass transfer, which is caused by conductive, convective and radiative heat transfer. Therefore, calculating an evaporation process, as shown in Figure 3.10, simplifies to an equilibrium of the vapour mass flux (or heat flux respectively) between the drop surface and the surrounding far field.

Star-CD assumes that the multiple components are uniformly distributed. From the provided fuel mass fraction Y_i, see Table 3.2, the corresponding mole fraction is determined. The vapour pressure curves provide the values of the saturation pressure p_i^0.

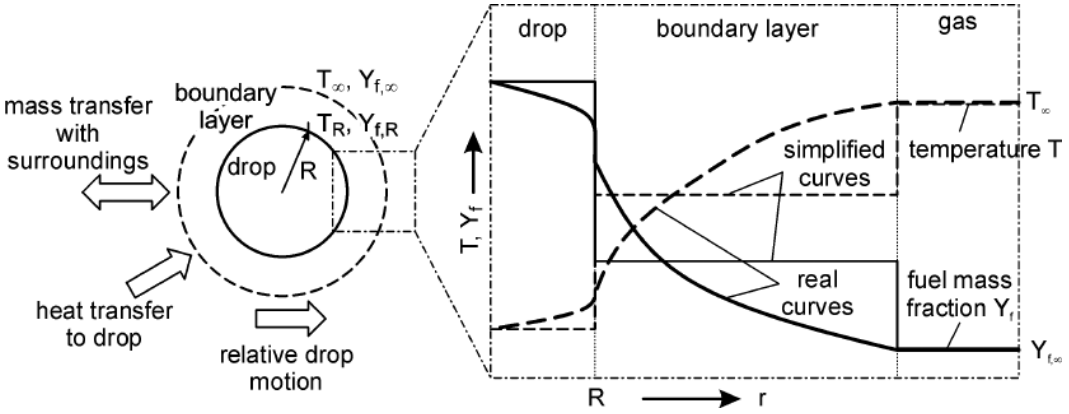

Figure 3.10: Schematic processes in drop evaporation, with the corresponding temperature and mass fraction curves in reality and under model assumption. Reprinted from Baumgarten [15] pp.139.

Therefore, partial pressure of an ideal mixture follows from Raoult's law:

$$p_i = X_{i,l} p_i^0 \tag{3.14}$$

Here $X_{i,l}$ describes the molar fraction in the liquid phase, p_i is the partial pressure of component i at the liquid-vapour interface, and the p_i^0 saturation pressure of component i. This correlation ensures that more volatile components of the droplet evaporate earlier than the heavier ones and therefore, mixture decomposition is predicted. According to the STAR-CD Methodology [18], multicomponent droplet vaporisation is determined by the following equation:

$$\frac{dm_{d,i}}{dt} = -\varepsilon_i \frac{Y_i}{\sum_{j=1}^{N} \varepsilon_j Y_j} A K_g p_t \ln \frac{(\varepsilon_i p_t - p_{vi,\infty})}{(\varepsilon_i p_t - X_{i,l} p_{vi,s}^0)} \tag{3.15}$$

Herein ε_i is a saturation proportion, A is the droplet surface area and p_t is the gas pressure. K_g is the mass transfer coefficient determined by the Ranz-Marshall correlation.

Details on the derivation of equation (3.15) are given in Glassman [25] and Abramzon et. al. [26]. Different thermodynamic states are also accounted and can be reviewed in the STAR-CD Methodology [18]. If the instantaneous mass transfer rate is known, the corresponding heat transfer rate source term, arising in the energy equation (3.13), is determined.

Collision and Coalescence was not considered in the subsequent investigations, although a model for these phenomena is provided in *STAR-CD*, for more information see Methodology [18]. Droplet collision and coalesce models provide known issues in solution stability and therefore, these phenomena are neglected. This assumption is valid, since in engine applications a fuel spray produces a high amount of small droplets, which evaporate fast before they may have the chance to collide.

3.5.4 Turbulent Dispersion

Depending on size, mass and velocity, fluctuations of the surrounding gas phase influence the moving path of the parcel, see Baumgarten [15] pp.169. Turbulent velocity fluctuations of the gas flow cause additional dispersion or diffusion of the liquid phase and therefore, increase the mixing rate of air and fuel. Smaller particles are captured by the eddies and follow the gas motion. Their interaction is then determined by the eddy life time. Large drops are not affected by the fluctuations and travel through, whereas intermediate ones are only affected by large-scale vortex structures. The additional momentum transfer is accounted for by assuming that the velocity fluctuations $\vec{u}'$ are isotropic and obey a Gaussian distribution. For a given drop velocity $\vec{u}_d$, the change in drop motion is then determined by calculating a corresponding velocity fluctuation according to equation (3.16). This fluctuation is a function of the interaction time τ_I, which follows as the smaller one of either the eddy lifetime τ_e or the transient time τ_t (time to pass through an eddy).

$$G'(u') = \frac{1}{\sqrt{\pi \frac{4k}{3}}} \cdot \exp\left(\frac{-|\vec{u}'|^2}{\frac{4k}{3}}\right) \tag{3.16}$$

In return, an additional source term arises in the gas phase turbulent k and ε equation, which influences the velocity of the following drops.

3.5.5 Spray Impingement and Liquid Film Formation

Liquid film formation and evolution has a high impact on mixture preparation and also the pre-ignition tendency of an engine. In order to properly determine the wall-film formation process, droplet impingement on the cylinder liner or the piston crown has to be modelled first.

Effects of Heat Transfer

Since both, droplet-wall interaction and the liquid film dynamic depend on the wall temperatures, the nonlinear liquid-solid heat transfer has to be introduced first. Between several heat transfer regimes, presented in Figure 3.11, is distinguished.

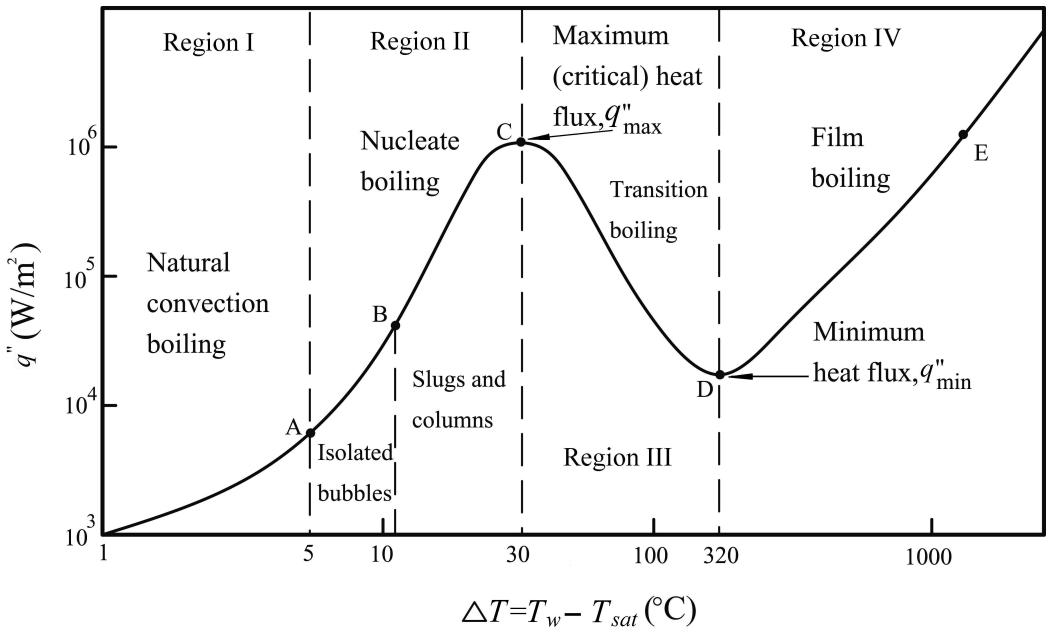

Figure 3.11: Nukiyama pool boiling curve for saturated water. Figure reprinted from [27].

In Region I and II, a liquid film is formed, which evaporates and bubbles emerge from the surface due to nucleation. Point *A* indicates the first formation of bubbles and point *B* corresponds to the point, where the bubbles first start to interact with each other. With increasing temperature, also the bubble density increases with the consequence that the slope of the boiling curve reaches a maximum value at point *C*. The corresponding temperature is called the Nukiyama temperature. Beyond this temperature in Regime III, the increasing number of bubbles form a multitude of continuous vapour films. If the temperature is high enough that a stable vapour film sustains (Leidenfrost temperature), the heat flux reaches a minimum value in point *D*. A thin vapour cushion insulates the liquid from the heated surface. Above the Leidenfrost temperature, in Region IV, phase change occurs at the liquid-vapour interface and the surface heat flux becomes a monotonically increasing function.

Spray Impingement

Droplet impingement on a surface does not necessarily lead to wall-film formation, see Figure 3.12. This rather depends on the fluid properties, the droplets kinetic energy and particularly on the wall temperature. Therefore, the Weber number and the Laplace number of the impacting droplet is used to classify different impingement mechanisms. The Laplace number is a measure for surface tension and viscous forces acting on the liquid:

$$We = \frac{\rho_l u_n^2 d}{\sigma} \qquad La = \frac{\rho_l \sigma d}{\mu_l^2} \tag{3.17}$$

u_n is the velocity component of the droplet normal to the impacting wall, σ its surface tension, and μ_l is the dynamic viscosity of the liquid.

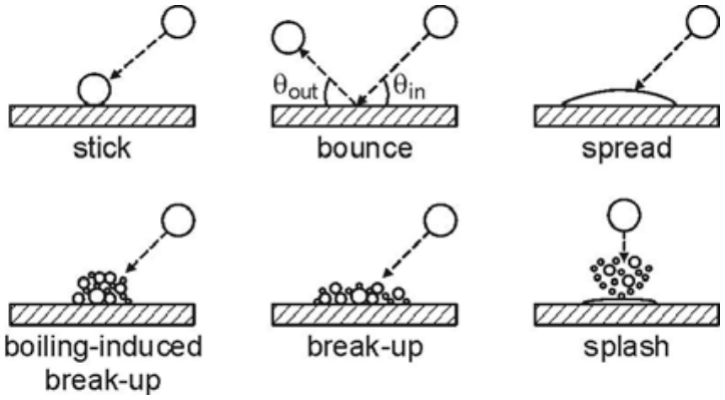

Figure 3.12: Impingement modes of a single droplet, reprinted from Bai et. al [28].

At low Weber numbers and wall temperatures, the drop may adhere/*stick* to the wall in nearly spherical form and evaporate. *Bounce* happens at dry but hot walls near Leidenfrost temperature, the droplet bounces off the wall as a vapour cushion prevents direct contact. With increasing Weber number, a complete *spread* out of the drop occurs forming either a wall-film or a mixture with an existing film.

At wall temperatures near the Nukiyama temperature, the drop heats up immediately, leading to break-ups into smaller droplets through boiling (*boiling-induced break-up*). In *break-up*, the droplet spreads out into a liquid film, but this film breaks-up into small droplets due to thermo-induced instabilities. If splashing happens, the drop partly adheres to the wall, but due to its high kinetic energy it becomes unstable and breaks-up.

In engine applications, the wall temperatures are in the range of the fuel's boiling temperature. Therefore, all these different impingement regimes are relevant and have to be regarded. The *Bai and Gosman* [28] droplet-wall interaction model is a multi-regime impingement model, which also differs between dry and wetted walls. This model classifies the impingement event according to three temperature levels and Weber number regimes, as depicted in Figure 3.13.

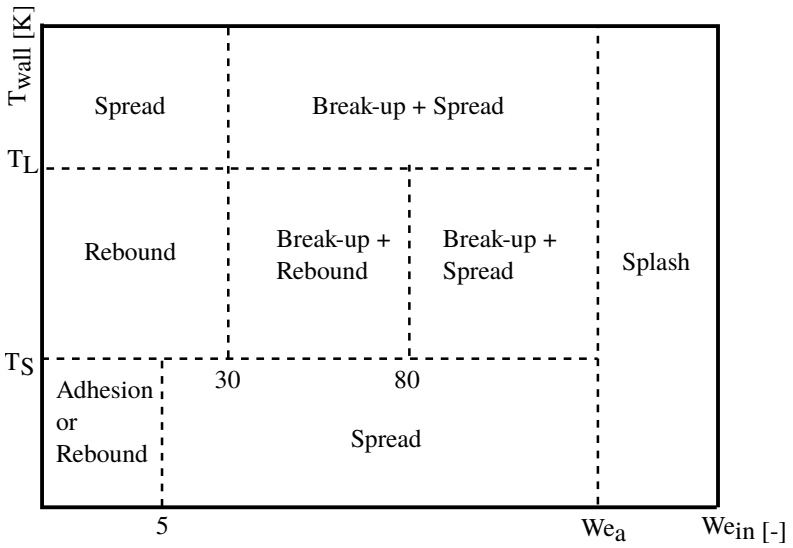

Figure 3.13: Impingement Regimes according to Bai and Gosman [28] as implemented in *STAR-CD*.

According to these classifications, *STAR-CD* determines the post-impingement characteristics of the droplet using different empirical correlations as well as mass and momentum conservation, see Methodology [18].

3.5.6 Liquid Film Modelling

In the case that a parcel adheres at the wall, it is assumed that the droplets spread out into a cylindrical form along the wall. Once enough droplets adhere at the wall and cover a certain area, *STAR-CD* decides on the basis of transition criteria if a liquid film is formed. Liquid film dynamic models are introduced at this point to predict the liquid film behaviour.

Mass, momentum and enthalpy conservation of each fuel component has to be ensured in *eulerian* description (see Section 3.5). Droplet impingement $\dot{m}_{in}$, film secondary break-up $\dot{m}_s$, and film evaporation $\dot{m}_{vap}$, see Figure 3.14, are considered in these equations via additional source terms, similar to the

spray source term. T_w wall temperature, T_{LF} liquid film temperature and T_f the incoming droplet temperature contribute to energy conservation.

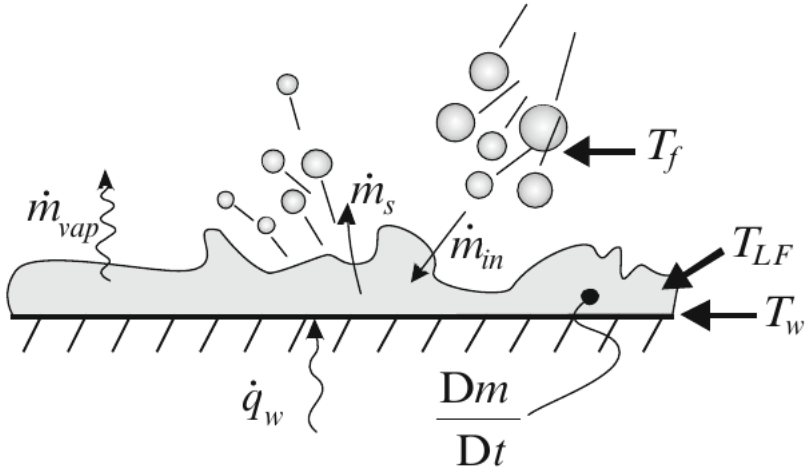

Figure 3.14: Liquid Film temperatures and heat fluxes as well as mass transfer sources/sinks contributing to mass conservation $\frac{Dm}{Dt}$, Figure reprinted from Ashgriz [16]pp.449.

The conditions at the surface between liquid film and gas phase is ensured by transition criteria according to Torres et. al [29].
The liquid film model implies the assumption that the liquid film is thin enough for the boundary layer approximation to hold. A parabolic velocity profile is assumed, and the temperature profile is piecewise linear. The condensation/evaporation rate of a liquid film is modelled for each component of the liquid film, and therefore also mixture decomposition is predicted. *STAR-CD* accounts for post impingement events (film stripping models), depicted as $\dot{m}_s$, which are basically mechanisms, where droplets detach from the liquid film due to either wave instability, instabilities resulting from body forces (gravity, piston acceleration) or break-up by flow over a sharp edge (intake valve seat). Dependent on the wall temperature, several classifications according to different temperature levels are conducted, which take the nonlinear heat transfer rate, see Figure 3.11, into account. Regime transitions are based on empirical nonlinear correlations for a minimal and a maximal heat flux. More information on the numerical implementation and the corresponding correlations are provided in the Methodology [18].

3.6 Geometry Change during Runtime

Moving meshes can be handled within *STAR-CD*s additional tool *es-ice*. This tool allows meshing of combustion engine geometries and applies in interaction with the solver routine *Pro-Star*. Key functions of geometry changes during runtime are the interaction of two different algorithms:

1. Boundary Movement
2. Mesh Redistribution

Boundary movement is incorporated by an additional differential equation that has to be solved simultaneously with the governing conservation equations. In this case a so called '*space conservation equation*' determines the grid position as an explicit function of time.

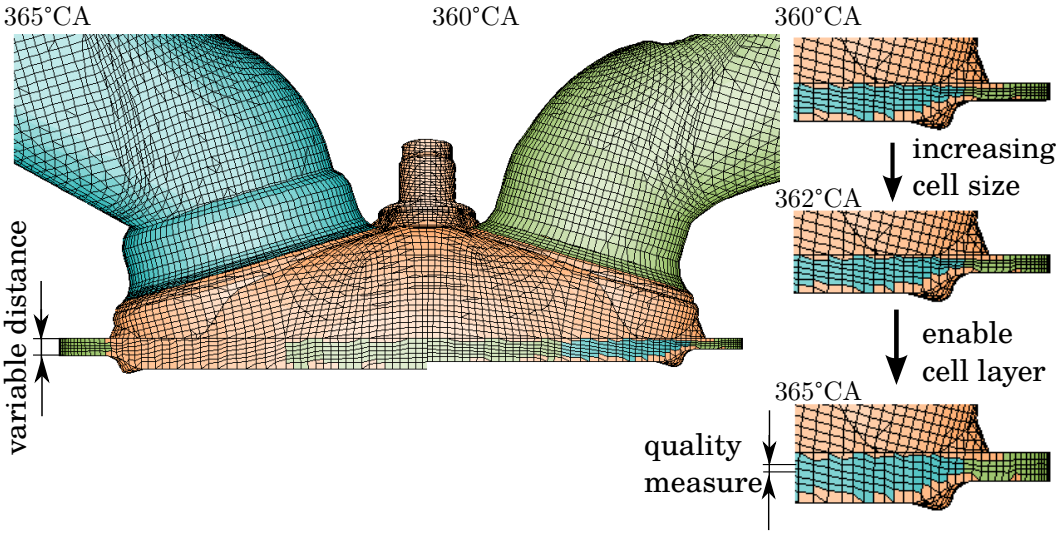

Figure 3.15: Moving mesh of an combustion chamber model.

According to the *STAR-CD* Methodology [18], this equation relates the change in cell volume to the cell face velocity. Therefore, all convective fluxes in the conservation equation are given as a function of the relative grid velocity. After boundary movement, the inner mesh vertices have to be redistributed, in order to ensure that no distorted or bad quality cells are formed.

According to *STAR-CD*, the redistribution algorithm is split into two parts. First, the vertices are redistributed to ensure good cell quality. Second, if the cell ratio exceeds a certain quality measure, cell layers attached to a boundary

can successively be enabled or disabled, see Figure 3.15. Disabled cells are stored in the background, ready to be enabled again in reversed order. Since the grid position is available as an explicit function of time, good cell quality can be ensured during the whole simulation. However, a mesh has to fulfil some restrictions such as uniform cell shape, orthogonality and smooth transition between smaller and bigger cells, in order to allow for enabling, or disabling cells.

Last, but not least, the solution determined by use of the *'old mesh'* has to be equally mapped onto the new one. This algorithm is numerically the more challenging one, since special care has to be taken, in order to ensure conservation of mass and momentum.

4 Bomb Experiment Studies

Since injections are highly transient and non-linear processes, it is necessary to adjust the numerical set-up precisely to measurement data. The measurement set-up is constructed of a quadratic chamber (called *"bomb"*), which is equipped with various measurement devices. To guarantee undisturbed spray development, the fuel is injected into a quiescent surrounding. Comparability between different measurement data is ensured by conducting *standard conditions for temperature and pressure*. In physics, only the liquid core and some ligaments exist directly at the nozzle exit. Therefore, drop size measurements are taken 30 mm below the nozzle exit. From *Phase Doppler Particle Analyzer (PDPA)* measurements the *Sauter Mean Diameter (SMD)* as a function of time 30 mm below the injector nozzle, is known. This measuring position is depicted in more detail in Figure 4.1.

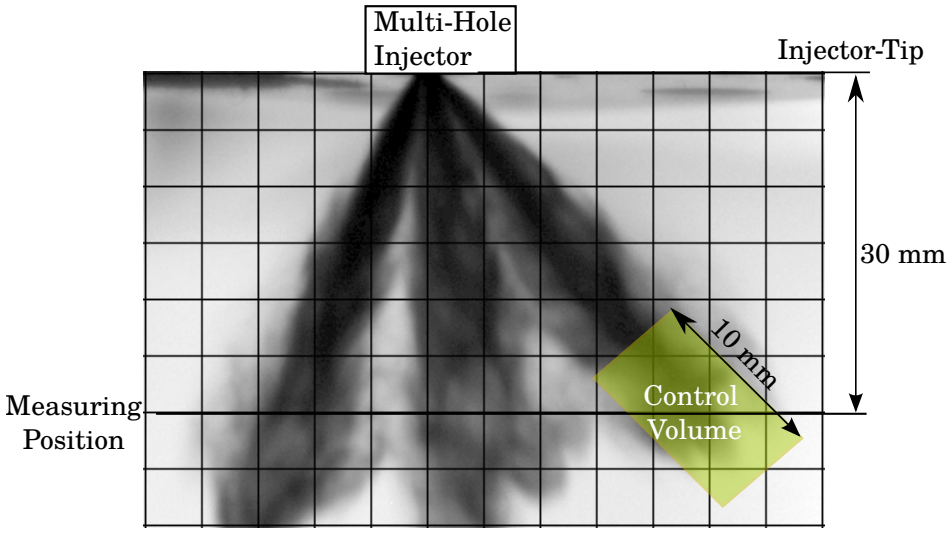

Figure 4.1: Spray parameter measuring position.

PDPA results at 200 bar rail pressure and an injection duration of 1 ms provide information on the mean drop size evolution and a mean spray velocity over time at the measuring position. Furthermore, high speed images of the spray

development are used to determine the spray tip penetration.
The goal of the bomb simulation is to meet the essential parameters in spray characterization, which are defined as:

1. Overall mean drop diameter (at 30 mm): 20.37 µm
2. Mean drop diameter development in time (at 30 mm):PDPA-Data
3. Spray tip penetration: High-Speed images
4. Spray cone angle: 16°
5. Fuel mass/diameter distribution: no data provided

Within the CFD framework, the determination of SMD values at a similar position takes place by analysing the parcels within a control volume, see Figure 4.1. Several test simulations are necessary, in order to establish the appropriate model settings, which accomplish the correct drop sizes 30 mm below the injector, as well as the correct spray tip penetration.

Figure 4.2 displays the whole mesh and a cut through the mid-plane of the simulation set-up. The cell sizes in the vicinity of the injector are refined, in order to improve accuracy of the numerical simulation. The exact specifications are displayed in Table 4.1.

Table 4.1: Model properties of the Bomb.

Number of Cells	Cell Size Range	Time Step Size
1536128	0.625 mm - 5 mm	1E-5

It is known, that the *Discrete Drop Method (DDM)* has the disadvantages of high time-step and grid-size dependencies, see Merker [7] pp.351. To ensure that those problems do not arise when changing the application model, the chosen simulation set-up meets the same cell size (in the vicinity of the injector nozzle) and the same time-step size as it is applied in the combustion chamber investigations in Chapter 5.
The software package *Pro-STAR* is utilised for pre- and postprocessing and its associated solver routine *STAR-CD* is used to determine simulation results.
In order to apply numerical simulation strategies, the following model assumptions are implied: an ideal gas (air) and a molecular transport according to the

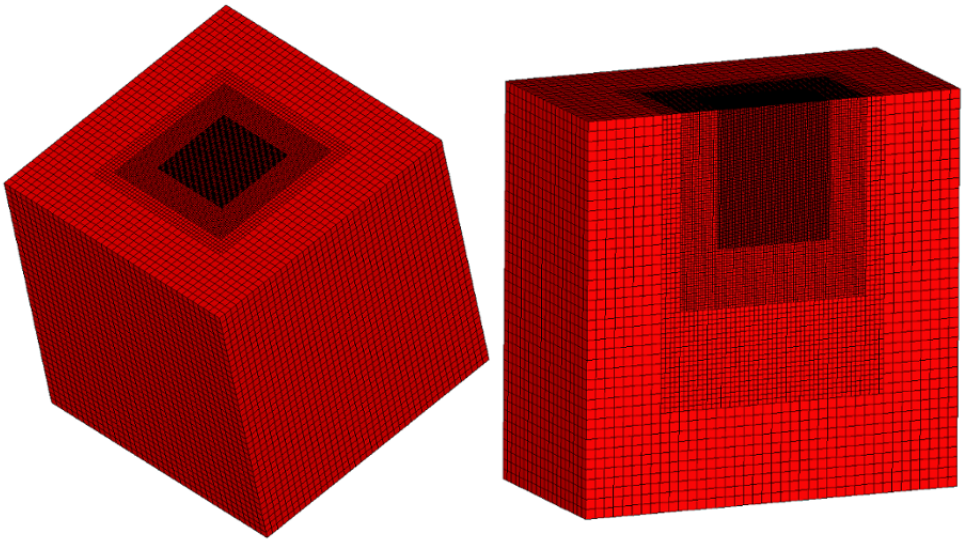

Figure 4.2: Mesh of the *Bomb* model under investigation. Left: whole mesh, right: section view onto the mid plain.

Sutherland-model are considered. Further, injection of the 7-component fuel, see Section 3.4, with independent vapour pressure curves is chosen to represent the boiling behaviour of real gasoline appropriately. The $k\varepsilon$ *RNG* turbulence model is applied for the gas phase. Turbulence is induced by the droplets via momentum exchange between liquid and gas.

4.1 Injector Properties and Boundary Conditions

The injector axes orientations, which are applied in the bomb investigations, are provided in Table 4.2. A corresponding illustration of these parameter is shown in Figure 4.3. This injector is also applied in the engine model simulation, later in Chapter 5.

By varying the numerical injection and break-up parameter, the simulation results are iteratively adjusted in order to meet the measurements.

Table 4.2: Orientations of the spray cone axes of the injector type under investigation.

	α_1	α_2	α_3	α_4	α_5	α_6
Variant 1	15.77°	66.08°	142.46°	-142.46°	-66.08°	-15.77°
	β_1	β_2	β_3	β_4	β_5	β_6
Variant 1	38.82°	22.09°	23.72°	23.72°	22.09°	38.82°

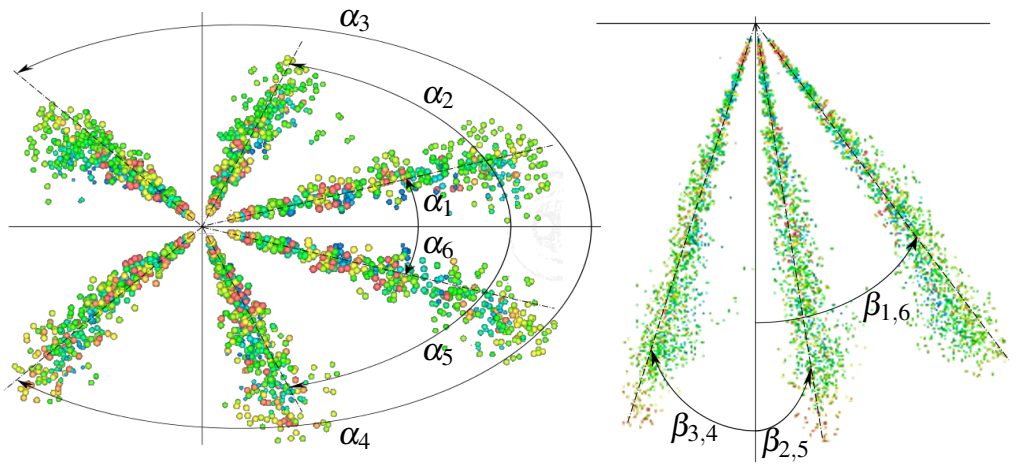

Figure 4.3: Orientation of the different injector axes, provided in Table 4.2.

The boundary conditions are summarized in Table 4.3. Whereas, the fuel rail pressure is incorporated indirectly. Dependent on the atomisation model, rail pressure is either considered in the prescribed mass flow rate or by an initial injection velocity in combination with the mass flow rate.

Table 4.3: Boundary condition for the simulation of the measurement set-up.

Ambient Temp.	Ambient Pressure	Fluid Temp.	Fluid Pressure	Injection Duration	Mass Flow Rate	Cone Angle	Injection Velocity
295.15 °K	1 bar	300 °K	200 bar	1 ms	17.5 $\frac{cm^3}{s}$	0-16°	143 $\frac{m}{s}$

Fluid properties and initial conditions are provided via individual user subroutines. Dependent on the corresponding injection model, additional data of either the nozzle hole geometry or the drop sizes, are provided.

Even though the injection duration, which is applied in the engine model, is longer, the bomb simulation is set up for 1 ms according to the available measurement data. This change is possible, since in a fully developed spray mean drop sizes in the *steady phase* remain at a constant value. This is called the *plateau value*, which is later visible in Diagram 4.2. This value remains until the end of injection, where smaller droplets follow, see Panao et al. [30]. For a longer injection duration, this plateau value takes place for a longer time. Therefore, it is sufficient to validate the spray parameters for 1 ms injection duration.

4.2 Investigated Break-up Models

The simulations are conducted by considering either primary or secondary break-up separately. In order to predict the atomization process at the nozzle exit, *Huh* primary break-up model is applied. This model uses general relationships to associate the injection parameters with the drop disintegration. Secondary break-up in contrast models droplet disintegration according to discrete Weber number regimes.

4.2.1 Primary Break-up

Primary break-up models are designed to take also the flow conditions inside the nozzle hole and especially at the chamber entrance into account. Therefore, some geometric data of the nozzle has to be provided.
In contrast to secondary break-up models, only the mass flow rate of the injector is necessary as a boundary condition. The model then determines the initial drop velocities itself.
At first, *Huh* standard model in its original form is investigated and then a second variant with adjusted nozzle discharge coefficient c_d is investigated thereafter. By decreasing this coefficient, the turbulence length scale is increased. Therefore, also the atomisation length scale and perturbation wave length is increased, resulting in an increase of parent drop sizes D_d (compare with Table 3.1). Simulation results are depicted in Figure 4.4. This view already reveals the increase in drop sizes due to the model adjustment.

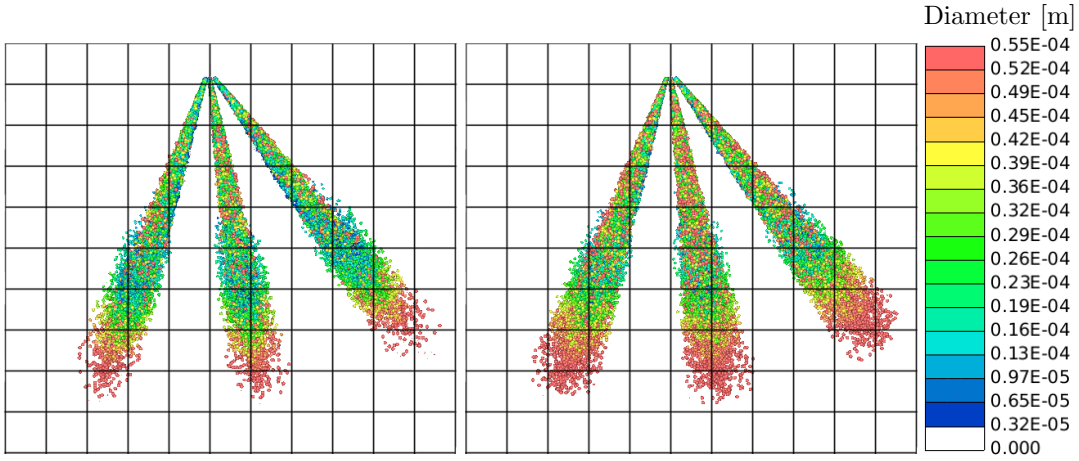

Figure 4.4: Primary break-up models at 0.46 ms. Left: Model with standard parameter. Right: Adjusted discharge coefficient c_d.

4.2.2 Secondary Break-up

In engine applications, atomization of the injected fuel takes place immediately at the nozzle exit. Therefore, it can be assumed that a liquid core can be neglected and only droplets exist within the chamber. This allows for prescribing a specific drop size distribution directly at the nozzle exit. The advantage of this methodology is that valid drop sizes are prescribed at the beginning and do not have to be calculated.
A measured drop size distribution of a similar injector with an initial *Sauter Mean Diameter SMD* of 20 µm is provided by the manufacturer. This distribution function is tested and simulation results are analysed at the measuring position.
When starting the injection process, the numerical code is first choosing a random diameter within the drop size distribution function. Then, a parcel is injected with a random velocity vector. The vector size is prescribed and the orientation is chosen within the provided spray cone angle range, depicted in Table 4.3.

The injection velocity is a key property in every injection process, but since the liquid flow directly at the nozzle exit is extremely dense and unsteady, no measurement data is available. A fast method for determining an approximation of the initial injection velocity, without carrying out expensive 3-dimensional simulations, is by balancing the calculated penetration of a single drop against a measured spray tip penetration. Within this methodology, a drop with a specified initial size and velocity is decelerated considering only aerodynamic forces.

$$F_{drag} = \frac{\rho_g}{2} u_d c_D A_d \tag{4.1}$$

With ρ_g the gas density, u_d the drop velocity, A_d the drop cross section and c_D the drag coefficient. This equation is solved by integrating the drop velocity numerically. Dependent on the Reynolds number, different correlations for the drag coefficient are determined.

$$c_D = \frac{24}{Re}\left(1 + \frac{1}{6} Re^{\frac{2}{3}}\right) \qquad Re \leq 1000 \tag{4.2}$$

$$c_D = 0.424 \qquad Re > 1000 \tag{4.3}$$

The resulting drop penetration is compared to measurement data. Deviations between those curves provide a measure for the chosen initial values. Diagram 4.1 shows a comparison of the calculated drop and the experimental spray penetration. An injection velocity of $143\,\mathrm{m\,s^{-1}}$, provided in Table 4.3, is determined via conducting this strategy.

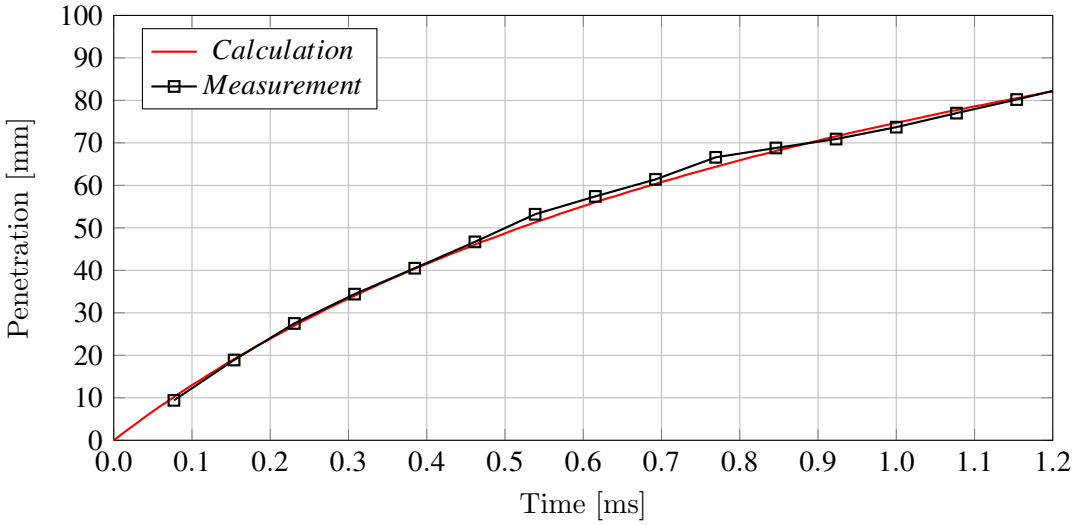

Diagram 4.1: Comparison of the measured spray tip - and the calculated droplet penetration.

The simulation results are presented in Figure 4.5 on the left hand side. Because of comparability reasons, the same colourisation scale as in the primary break-up model is used.
Since drop disintegration takes place immediately, directly at the nozzle exit, the resulting drop sizes do not correlate with the measurement data. However, by analysing the Weber number decrease between the nozzle exit and the measuring position, an estimation of a more realistic initial mean drop size distribution can be made. A second variant with raised, but otherwise equally distributed drop sizes is investigated (Inj. Variant 2).

Table 4.4: Weber number decrease of Inj. Variant 1 and the estimated Weber number decrease of Inj. Variant 2.

	init. SMD	init. We	SMD	We
Inj. Variant 1	20 µm	6.13	15 µm	1.94
Inj. Variant 2	36 µm	11.06	20.37 µm	3.5

Table 4.4 shows the parameter of Inj. Variant 1 by which the new initial mean drop size is estimated. The drop velocity (at the measuring position) of Inj.

Variant 1 is given by the simulation results. However, at the measuring position, the mean drop size should be 20.37 µm. A drop velocity there can be estimated by use of the one-dimensional analyses according to equation 4.1.With this knowledge, and the knowledge of the Weber number decrease, a new initial mean drop size can be estimated.
In order to regard a more intensified disintegration of bigger drops due to secondary break-up, the prescribed distribution function is raised from a mean value of 36 µm to a value 40 µm. The resulting spray shape of Inj. Variant 2 is shown in Figure 4.5 on the right hand side.

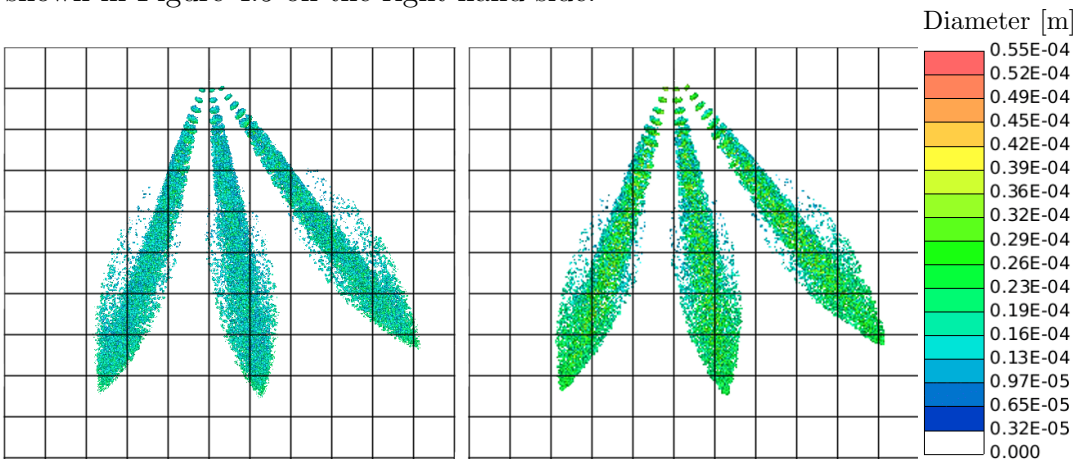

Figure 4.5: Secondary break-up models at 0.46 ms, left: Model with measured diameter distribution. Right: Adjusted diameter distribution.

In summary the investigated model set-ups, differ by the following factors: In Inj. Variant 1, a mean drop size distribution is initialised, which has the same *SMD* value as it is known from the PDPA-measurements. A second variant with raised, but equally distributed drop sizes is investigated in Inj. Variant 2. In order to properly predict the conditions at the nozzle exit, *Huh* primary break-up is investigated in Inj. Variant 3. An adjusted version, which enhances the formation of bigger drops, is finally investigated in Inj. Variant 4. A direct comparison is depicted in Table 4.5.

4.3 Comparison between Primary and Secondary Break-up

A validation process of the simulation results against measurement data provides information on the impact of the various atomisation models. When

Table 4.5: Different injection set-up variants in comparison.

	inj. Velocity	init. mass flow rate	init. SMD	Primary Break-up	Secondary Break-up	Model adjusted
Inj. Variant 1	143 $\frac{m}{s}$	0.01298 $\frac{kg}{s}$	20 µm	-	Reitz-Diw.	Standard
Inj. Variant 2	143 $\frac{m}{s}$	0.01298 $\frac{kg}{s}$	40 µm	-	Reitz-Diw.	Standard
Inj. Variant 3	-	0.01298 $\frac{kg}{s}$	-	Huh	-	Standard
Inj. Variant 4	-	0.01298 $\frac{kg}{s}$	-	Huh	-	$c_d = 0.4$

comparing the shape of the spray cones in Figure 4.4 and Figure 4.5, the differences between primary- and secondary break-up become clear. While primary break-up is concerned with the disintegration of the liquid core and the bigger droplets at the nozzle exit, this model is lacking in the prediction of aerodynamic forces onto drops. The whole spray is shaped like a sharp cone and no distinct spray tip formation takes place. Secondary break-up in contrast, is concerned with the disintegration of little drops into even smaller ones. Therefore, arrow shaped spray tips develop, which can be also observed at later stages in high-speed photographs.

In Diagram 4.2, a comparison between the mean drop sizes obtained by the simulation as well as by the measurement data is shown. From the measured evolution can be seen that the first drops, which leave the nozzle hole, have bigger sizes than the following ones.

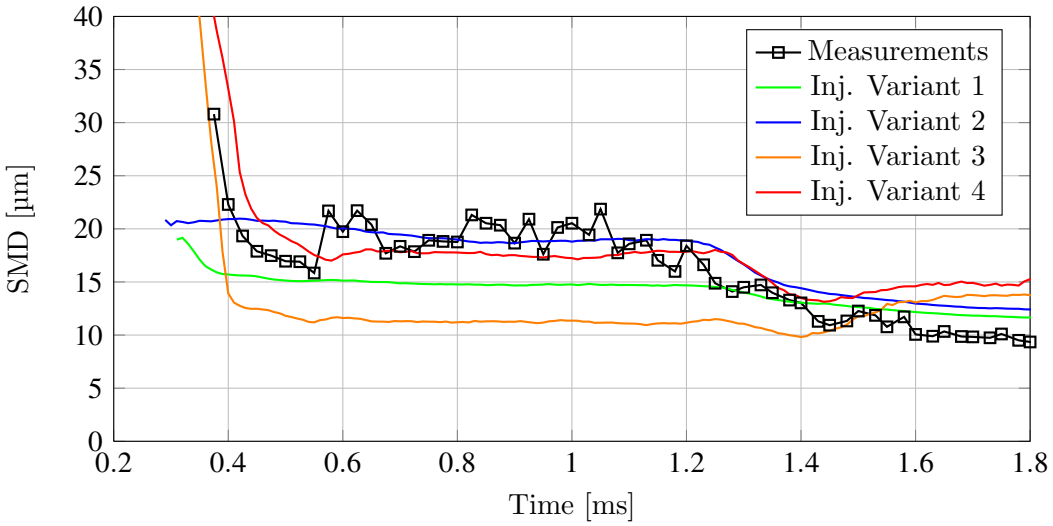

Diagram 4.2: Evolution of the mean spray drop diameter during time.

This is called according to Panao et al. [30] the *"leading front of the spray"*. Then a second period, where the drop sizes maintain at a constant mean or plateau value called the *"steady spray"*, is entered. This is the relevant spray phase, where simulation results have to fit to the measurements.

Diagram 4.2 indicates, that Inj. Variant 1 and 3 do not meet the measurements well, because their drop sizes instantaneously become too small. Except of the first value in Inj. Variant 2, a good agreement with the measurement data can be observed for this variant, as well as for Inj. Variant 4. One can see that the *leading front of the spray* cannot be predicted by initializing a drop size distribution at the nozzle exit, however, the *steady spray* phase agrees well. As reported in Malaguti [31], *Huh* primary break-up model produces very small droplets, this also agrees with the findings of this diagram. In accordance with the findings in Malaguti [31], secondary break-up had to be skipped at all, in order to meet the measurement data with the adjusted model set-up.

Not only the *SMD* development is of interest, but also the spray tip penetration is an important spray characteristic. This is shown in Diagram 4.3. One can see, that the spray tips penetrate at almost the same rate as in Inj. Variant 1 and 2. Also the penetration rate in Inj. Variant 3 and 4 is almost identical. Therefore, dependent on the break-up model, correlations in the penetration rates can be observed.

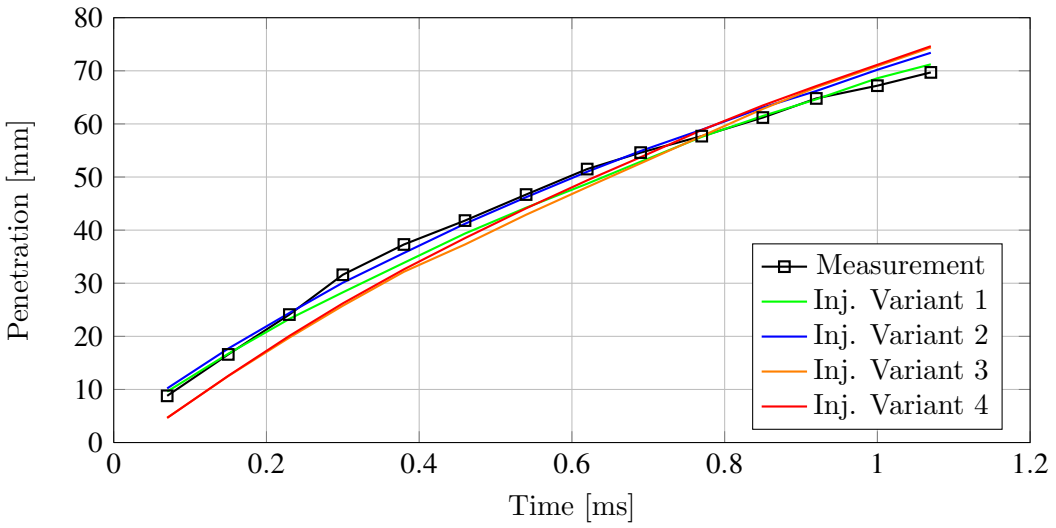

Diagram 4.3: Spray tip penetration of the measurements in comparison to the simulation results.

On average, Inj. Variant 1 and 2 agree well with the measurements and occurring deviations are within the error tolerance. At the beginning, variants, which adopt primary break-up remain behind the desired spray tip penetration. However, with ongoing injection duration, Inj. Variant 3 and 4 are able to catch up, and even pass the measurement trace. At the end, the slope of the curve indicates an overestimation of the spray tip penetration. But since for further penetration no measurement data is available, one is referred to observations in Malaguti [31].

A more precise picture on the differences between the break-up models can be obtained, if the drop size distribution at the measuring position 30 mm below the injector nozzle is evaluated, see Diagram 4.4. In order to determine the drop size distribution from the simulation results, a representative time of 0.7 ms is chosen. At this time the spray is already fully developed within the *"steady spray"* phase.
Since the initial drop size distribution of Inj. Variant 1 corresponds to measurements of a similar injector, this distribution is a reliable comparative for the simulation results. Therefore, this data is also depicted by the black line in Diagram 4.4.
When comparing these curves, it immediately stands out that variants, which adopt *Huh* primary break up model, do not even roughly meet the desired drop sizes.

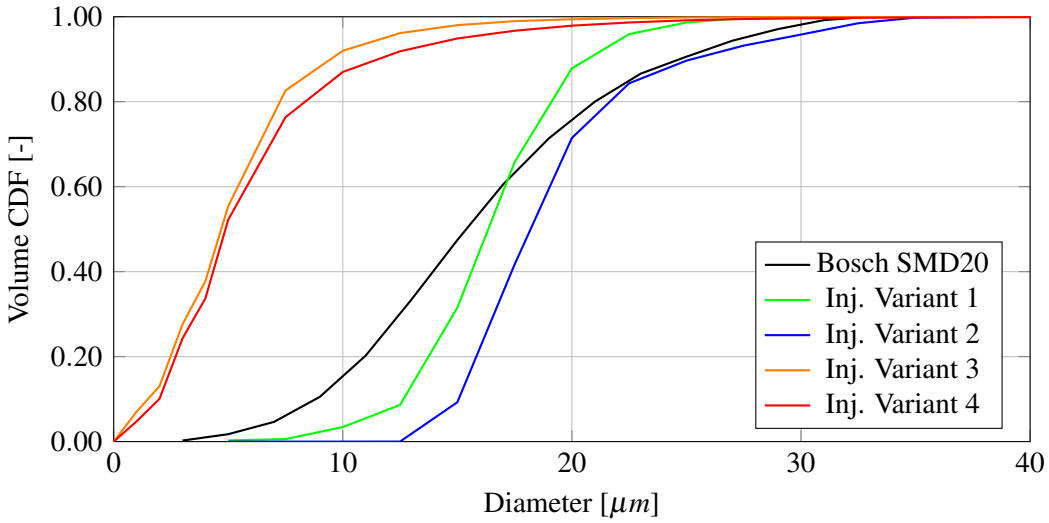

Diagram 4.4: Drop-size distribution at 30 mm below the injector.

Even though, the overall mean drop size of the adjusted model agreed in Diagram 4.2, the distribution function brings to light, that this is only explainable by a few specific big drops accompanied insufficient small ones.
However, the desired drop sizes should be distributed around a *SMD* value of 20.37 µm. As it was visible in Diagram 4.2, the drop sizes of Inj. Variant 1 are too small, in Inj. Variant 2 the percentage of bigger drops agrees well. Since the *SMD* value of ∼20.37 µm is in accordance with the known measurement data, the injection model set-up according to Inj. Variant 2 is superior and will be applied in the engine model simulations in Chapter 5.
Finally, for an optical evaluation high-speed shots are compared to the simulation results of Inj. Variant 2 at equal penetration times, see Figure 4.6.

Concerning the high-speed photographs, it is indicated that there was no information provided on the relative position between the camera and the injector tip. Therefore, it is not possible to define, which of the aligned spray cones is in front or behind. Additionally, no collimated light source was used. Both incidents can cause uncertainties in the measurement process.
Spray cones of the simulation are positioned congruent on top of each other. A comparison shows, that the principal spray shape, especially at the first half of the injection event, agrees well. Aerodynamic forces and turbulence spread the spray cone in the high-speed shot observations more intensely than in the simulation. With proceeding injection, a big cloud of small droplets and vapour is surrounding the dense spray axes.
However, simulation results do not show this droplet vapour cloud, only the dense spray axes. This is, on the one hand, explainable by the *DDM* approach. Only parcels are pictured. But one parcel represents a group of droplets with the same properties. On the other hand, no vapour cloud surrounding the spray cones, is depicted.

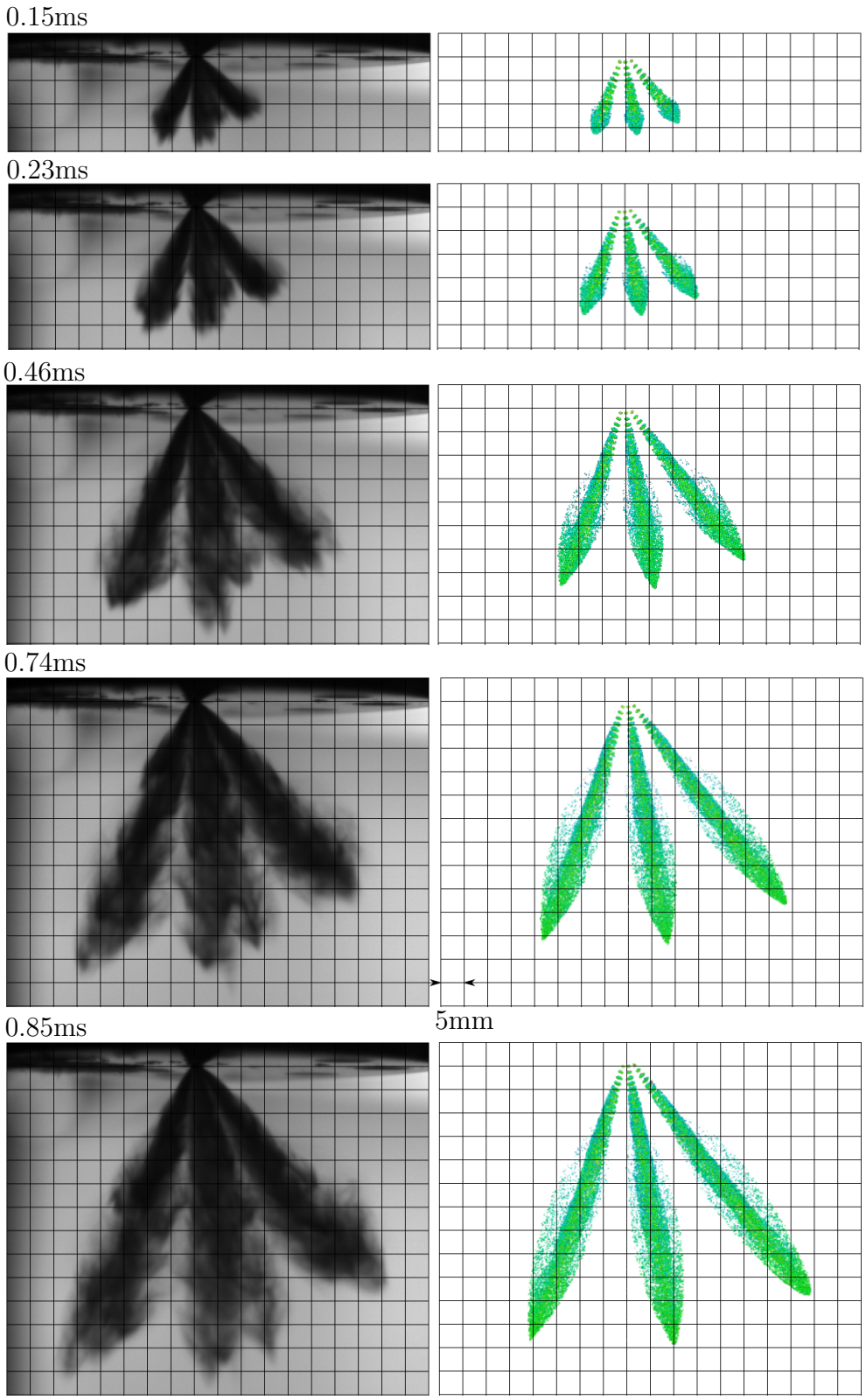

Figure 4.6: Penetration at 0.15ms, 0.23ms, 0.46ms, 0.74ms and 0.85ms in comparison. Left are the high-speed photographs, right the simulation results.

The main objective of the *Bomb* investigation is the validation of the spray set-up for the in-cylinder application against experimental data. In the previous findings, the simulation set-up with boundary conditions according to Table 4.3, and an initial drop size distribution with *Sauter Mean Diameter* of 40 µm, meets the measurement data best.
It has been shown that secondary break-up models show good tendencies to meet the required measurement data. Nevertheless, the presented observations show that there are significant differences between the drop size distributions initialized at the nozzle exit and the measuring position. Satisfying agreement could only be achieved by initialising a drop size distribution with distinct bigger drop sizes. This increases model set-up time, since the appropriate drop size distribution has to be determined iteratively.

Furthermore, one can see in Diagram 4.4 that the primary break-up model has issues in calculating drop sizes correctly. Even though the sprays mean *SMD* value is correctly predicted, the whole spray morphology does not meet the measurements. These results suggest, that primary break-up models in combination with secondary break-up might improve the gained results. However, in accordance to the findings in Malaguti [31], secondary break-up has to be limited, or even skipped, in order to avoid too intensive droplet disintegration. Therefore, primary break-up is no longer considered as a convenient model set-up is at the moment topic of current research.

All models have in common that a lot of tuning work is of great importance in order to represent the physical spray characteristics correctly. The chosen procedure provides the advantage that initial conditions already agree with measurement data. Therefore, deficits of the atomisation models can be avoided by promoting the physical properties of the spray, which are maintained in relevant areas.

5 Injection Processes Inside an Engine Model

On the basis of these preliminary testings in Chapter 4, an analysis of the injection process in a direct injecting combustion engine is performed. Different injector geometries and their impact on mixture preparation during the intake and compression stroke are investigated. Therefore, a model of one cylinder of the V6 Jaguar AJ126 engine, is created and set-up according to its shape and physical operating conditions. Its specifications can be reviewed in Table 5.1. This light weight structured, supercharged V6 engine consists of an aluminium

Table 5.1: Engine data of the Jaguar AJ126.

Cylinder	Valves	Displ.	Bore	Stroke	Compr.	Power	Spark
290° V6	24	2995 cm^3	84.5 mm	89 mm	10.5:1	250 kW	−12.75°CA

alloy engine block with four camshafts, incorporating dual independent variable camshaft timing (CIVCT). It has four valves per cylinder, which are positioned in an aluminium DOHC cylinder head. A supercharger located in the 'V' of the engine and an inter-cooler take care of the charge air supply. Two high pressure pumps feed a *Bosch* high pressure injection fuel system, whose different injector types are part of the subsequent investigations.

5.1 Mesh Generation and Model Set-up

The CFD analysis is based on a provided cylinder mesh. This mesh is improved in order to realize several optimizations such as inserting the detailed geometry of the spark-plug and the injector. The final mesh contains ∼1.4 million cells at BDC. Mesh refinement around these segments is necessary to ensure an accurate resolution. Figure 5.1 shows the whole mesh (left), and a detailed section view through the spark plug and the injector (right). *CD-adapco's* software tool

es-ice version 4.16 is used for the remeshing and boundary condition assignment. After the meshing process, the simulation set-ups are finalized in the software tool *pro-STAR*, before the solver *Star-CD* version 4.18 executes the simulation.

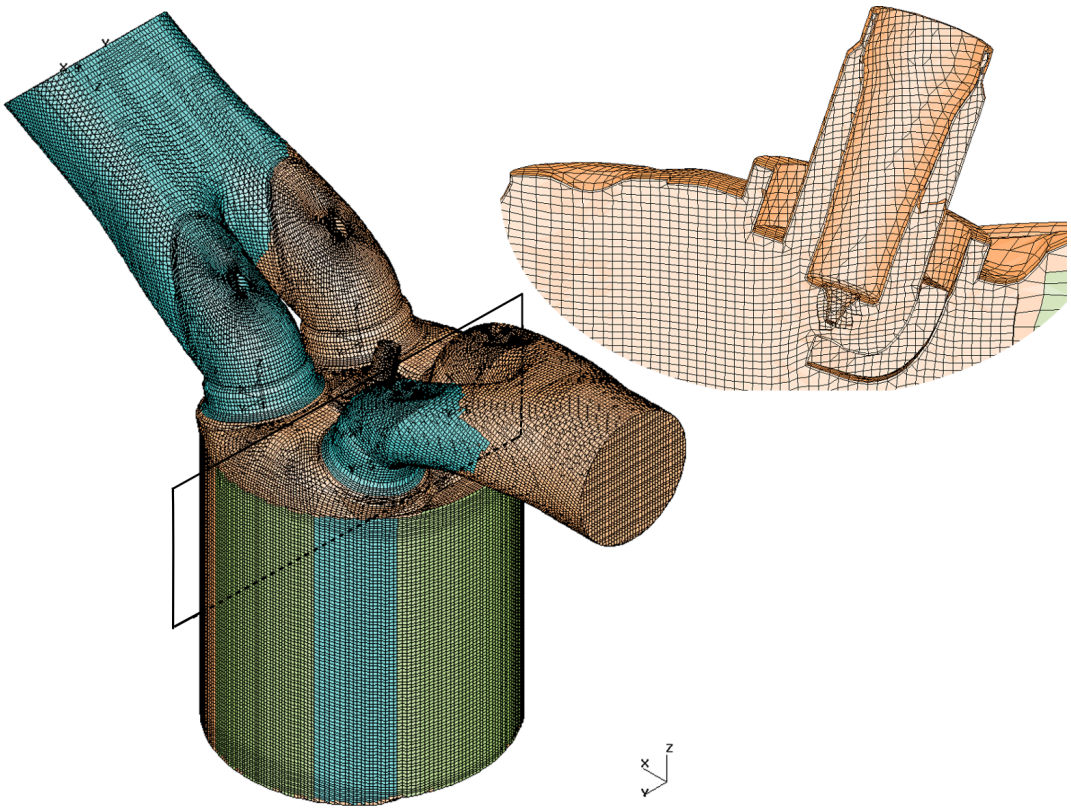

Figure 5.1: Mesh of the cylinder and the refined detail of the spark-plug and the injector tip geometry.

Two different injector configurations, which were provided by the manufacturer, are investigated. The detailed orientation, which corresponds to Figure 4.3, is

Table 5.2: Nozzle hole orientations of the two injector types under investigation.

	α_1	α_2	α_3	α_4	α_5	α_6
Variant 1	15.77°	66.08°	142.46°	-142.46°	-66.08°	-15.77°
Variant 2	21.89°	65.54°	148.41°	-148.41°	-65.54°	-21.89°
	β_1	β_2	β_3	β_4	β_5	β_6
Variant 1	38.82°	22.09°	23.72°	23.72°	22.09°	38.82°
Variant 2	49.00°	39.55°	33.38°	33.38°	39.55°	49.00°

provided in Table 5.2. The polar angles β_i of Variant 2 are bigger, which lead to a shallow orientation of the spray axes measured from the cylinder dome. In Variant 1 the axes of the injector cones target steep into the cylinder.

The engine speed under investigation is at $3000\,\mathrm{min}^{-1}$. The corresponding boundary and the initial conditions are determined by one-dimensional simulations using the software tool *GT-Power*. As inlet boundary condition the mass flow into the intake port is prescribed, while a fixed pressure is used as outlet boundary condition. A comparison between the mass flows determined with GT-Power and the CFD simulation is provided in Figure 5.2.

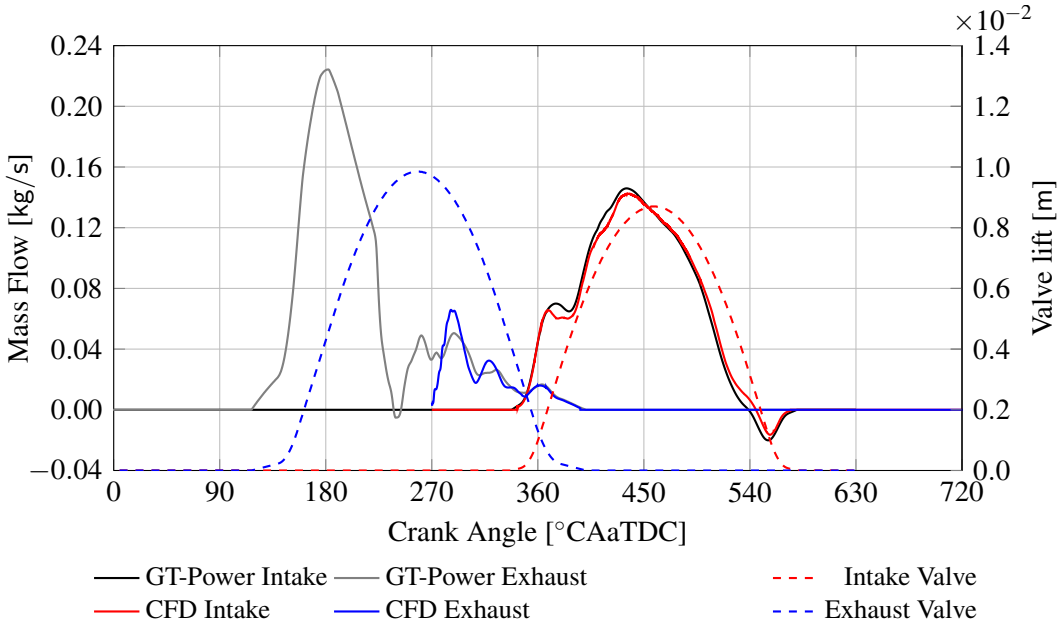

Figure 5.2: Mass flow determined by CFD and GT-Power and the prescribed Valve lift function at $3000\,\mathrm{min}^{-1}$.

Except for the injection duration, boundary and initial conditions of the injection event are the same as in Chapter 4. However, the ambient conditions are now determined by the simulation. The parameters of the injection event are summarised in Table 5.3.

Table 5.3: Injection parameters of the in-cylinder model.

Inj. Fuel Mass	Start of Inj.	End of Inj.	Inj. Pressure	Inj. Parcels	SMD
70.889mg	410°CA	496.6°CA	200bar	100 000	40µm

For the ambient gas field the kε/RNG turbulence model is used. Cavitation and other effects inside the nozzle hole are neglected and *Primary Break-up* is skipped, due to the assumption that the injection takes place within the atomization regime.

Only the *Reitz-Diwakar* secondary break-up model is used, while droplet-wall

interaction is considered via the *Bai and Gosman* model. The 7-component fuel model, presented in theoretical background in Section 3.4, is used to investigate the mixture preparation and wall-film formation tendencies.

In particular, specific wall-film formations and their location before ignition timing are of interest. Since these factors contribute to the pre-ignition tendencies of the engine, see Section 3.1, an evaluation of the influences arising due to different spray axes orientation, as well as the differences arising due to varying injection, parameters are of great interest.

5.2 Influence of Different Injector Types on the Charge Motion

Tumble is referred to as the large scaled gas motion generated by the intake air motion. The flow passing the inlet valves is forming a jet moving down the cylinder liner, across the piston crown and up the liner walls at the intake valves side, see Figure 5.3. This organised motion gradually breaks down to turbulence.

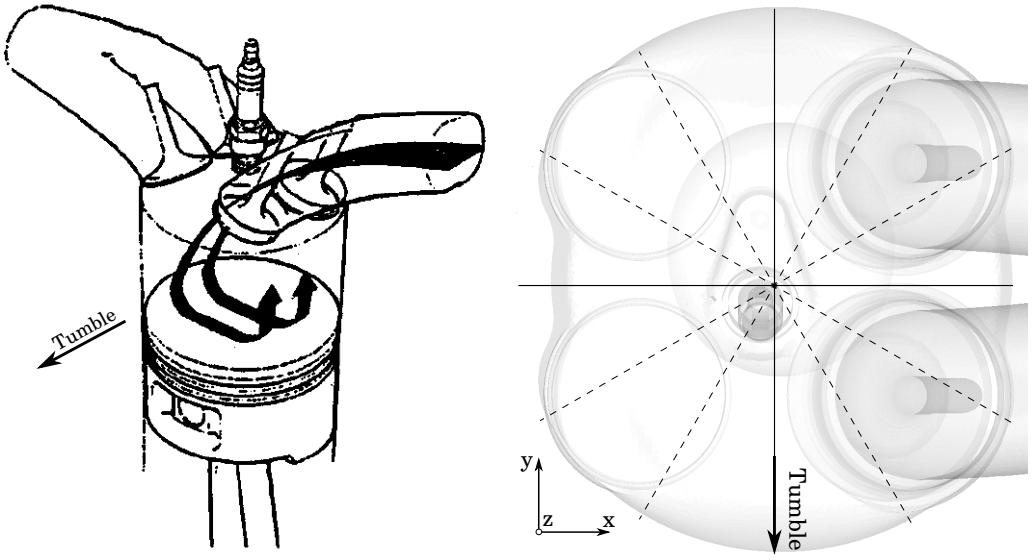

Figure 5.3: Tumble Motion, left picture reprinted and modified from Lumley [32].

Therefore, flow properties as well as their constituent components e.g. fuel vapour, droplets and residual gases are transported within the combustion

chamber and mix. During compression, turbulence decays and as density increases, dissipation raises due to viscosity as well.
Following Lumley [32], the bulk of organised gas motion breaks up into turbulence, since available space is getting constantly smaller as the piston arrives at TDC. Some of the organised motion survives, but it then gradually disintegrates into turbulence accelerating the flame velocity during combustion. During power stroke, the remaining tumble motion finally approaches zero.

By comparing the dominant velocity scales, dimensionless indicator quantities can be determined. These velocity scales are the flow velocity and the size of the crank shafts angular velocity. The flow velocity is determined by considering the solid-body rotation around the y-axes with the same angular momentum as the actual velocity distribution. The ratio of these quantities leads to the so called "Tumble number", see Figure 5.3.

Dependent on the intake design, various flow structures become dominant, since in the Jaguar AJ126 no distinct measures are taken, to enhance the intake flow, the tumble ratio is relatively low. Diagram 5.1 shows the tumble number with respect to the crank angle position during intake and compression stroke.

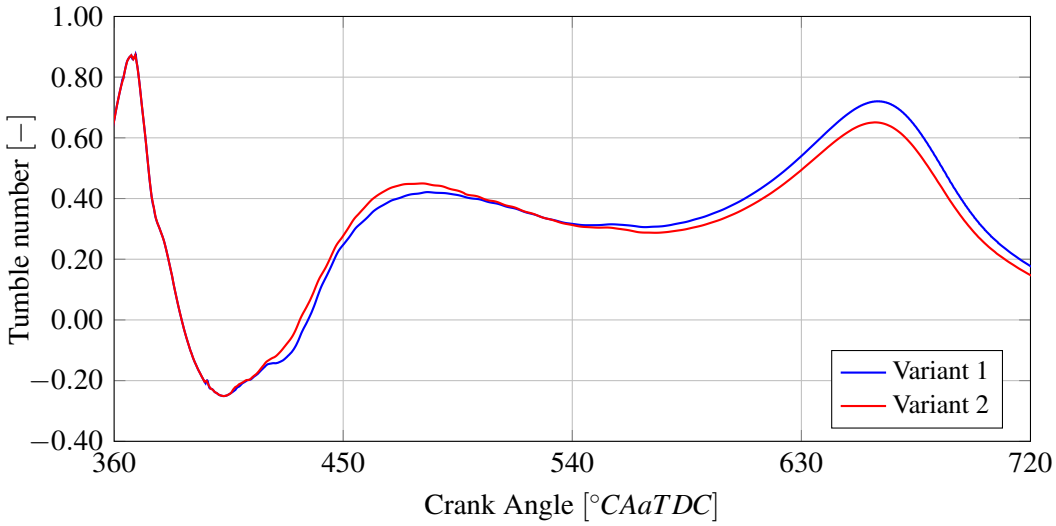

Diagram 5.1: Tumble number during intake and compression stroke.

Differences between the injector variants remain small during the whole intake and compression process. This is because only the injector axes orientation varies. However, Diagram 5.1 confirms that the injector types have an impact

on the charge motion. Therefore, mechanisms which lead to these deviations are of great interest and are now investigated in more detail.
In general, a high tumble ratio is desirable, as the intensified turbulence guarantees homogeneous mixing.
The first peak at about 380°CA is reasoned in the high intake velocities during the valve-opening overlap. With closing exhaust valves the tumble ratio decreases rapidly. The intake flow as well as the down going piston accelerate the cylinder charge and as soon as a stable vortex motion develops, the tumble number increases. With start of injection (SOI), the Tumble ratio of Variant 1 is deviating from that of Variant 2.

This is reasoned in the different spray axes orientations. Because of their high momentum, the steep into the cylinder penetrating droplets of Variant 1 act like a barrier for the intake gas. Therefore, the drops promote the intake jet first, but as the flow reaches the piston crown, the airflow is decelerated, see Figure 5.4.

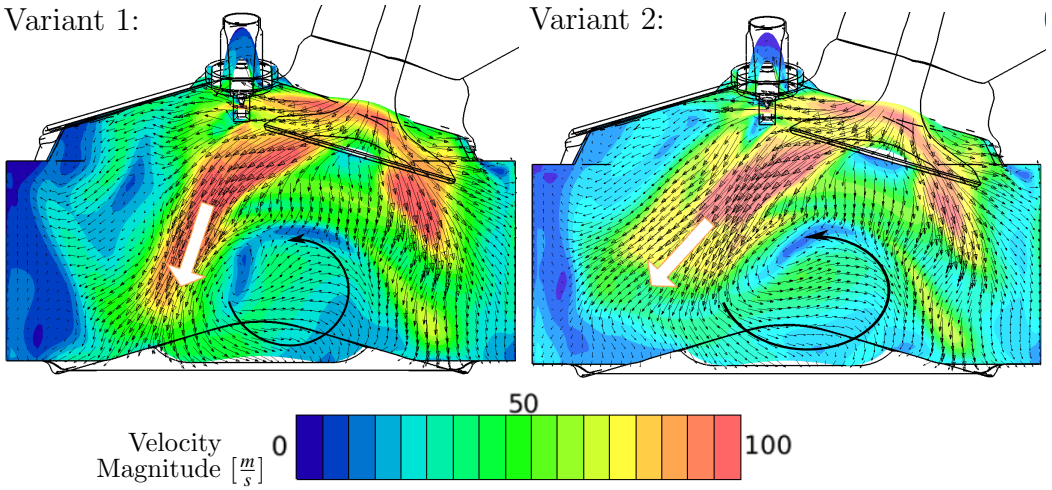

Figure 5.4: Velocity vectors and velocity magnitude at 426 °CA.

When comparing the velocity distribution at 426 °CA, the differences between the two variants become clear. The tumble vortex of Variant 1, depicted in black, is ”locked” between the intake gas jets. Therefore, large areas remain with small velocities. In Variant 2 in contrast, the intake flow has more space available, accelerating the whole cylinder charge in a more uniform way. Therefore, a stable vortex motion develops earlier, which increases the tumble ratio.

As the intake phase continues, the increasing moment of inertia causes a decrease in the tumble ratios and the curves align almost when the piston enters BDC. As the piston moves up again the charge motion is accelerated, while the moment of inertia decreases. Therefore, kinetic energy increases, elevating also the tumble number. The two tumble traces again deviate, but now Variant 1 has a higher tumble number.
The flow structures within a vertical section ∼20 mm in front of the injector at 580 °CA are pictured in more detail in Figure 5.5. While for Variant 1, the flow is streaming within a global vortex shape along the whole cylinder height, in Variant 2, two counter-turning vortices have developed, interfering with each other. Therefore, dissipation of kinetic energy is increased within this area, causing the sustained deviations between the tumble traces.

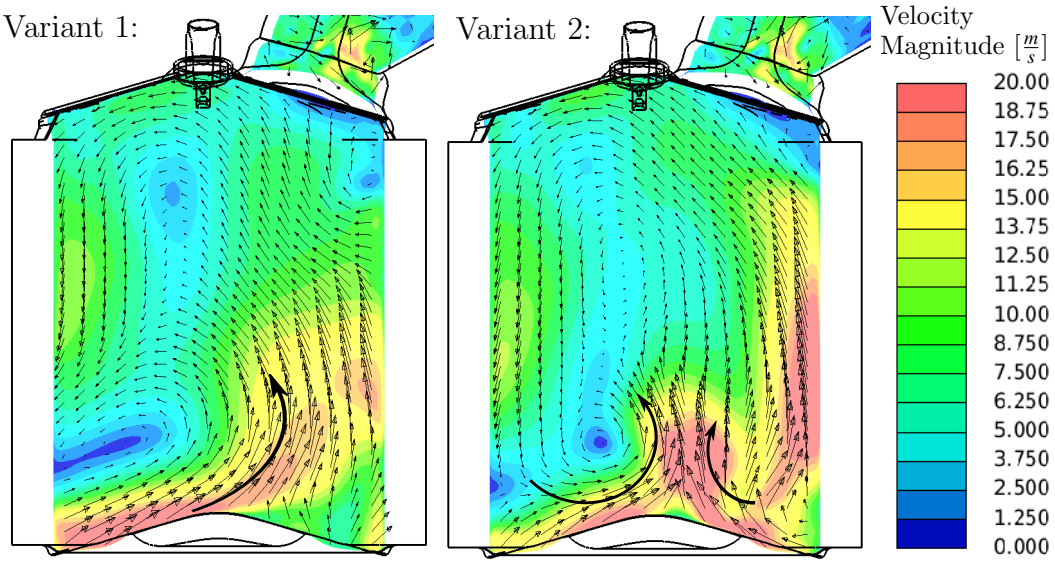

Figure 5.5: Velocity vectors and velocity magnitude at 580 °CA.

A similar picture can be drawn when reviewing the mean turbulent kinetic energy evolution, see Diagram 5.2. As the intake flow in Variant 1 is intensified by the spray, more turbulent kinetic energy is generated during the intake stroke. In Variant 2, tumble becomes higher during intake, but the kinetic energy is converted into turbulence during compression. Therefore, the turbulent kinetic energy level of both variants remain at the same level. Additional energy input due to piston moving is constantly dissipated, which keeps the turbulent kinetic energy level almost constant. Ignition timing is located around the local maximum right before TDC. Thereafter, the remaining turbulence dissipates

relatively fast, because of the high mixture density and the limited space. One can see in Diagram 5.2 that even though the tumble is at the beginning higher in Variant 2, all its energy is dissipated and at ignition timing hardly any difference between the injector variants is left.

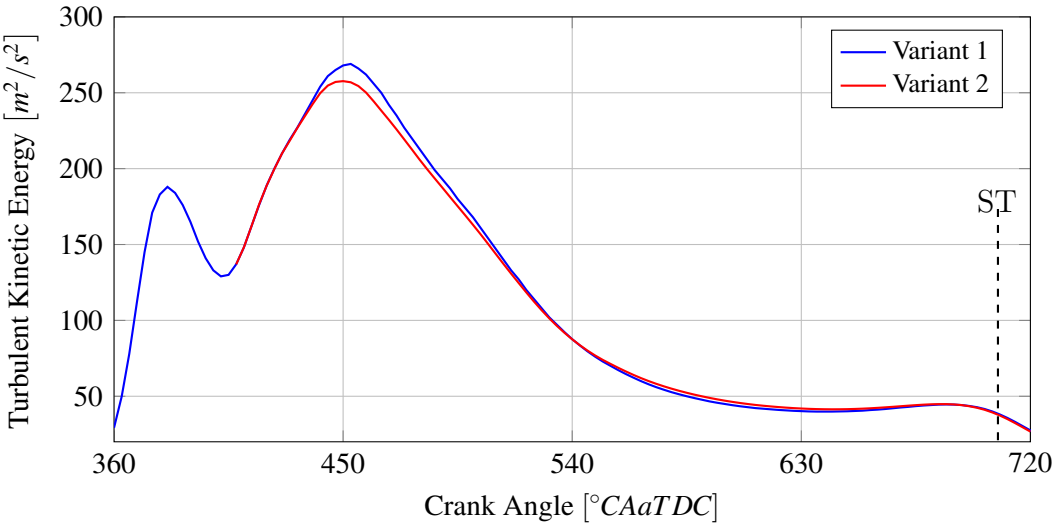

Diagram 5.2: Turbulent kinetic energy during intake and compression stroke, and spark timing ST.

5.3 Influence of Different Injector Types on the Mixture Preparation

Event though the charge motion itself has only minor impact on the pre-ignition tendency, it is of great importance for mixture preparation. Since the mixture is a result of turbulent flow field, spray timing and targeting, all these parameters have to be considered when investigating LSPI.

In the subsequent investigations, differences in wall-film formation and its detailed specifications are presented in order to determine the contributing factors on pre-ignition tendency of this engine. Vaporisation rate and therefore also the amount of liquid film formation differs, depending on the injector type and flow conditions.

During compression, and even during combustion, the bulk of wall-film has enough time to vaporise and burn. But this depends on the film specifications. If the liquid film becomes too thick, or if the film pools are located at the liner where the accumulations are collected by the up moving piston ring, abnormal

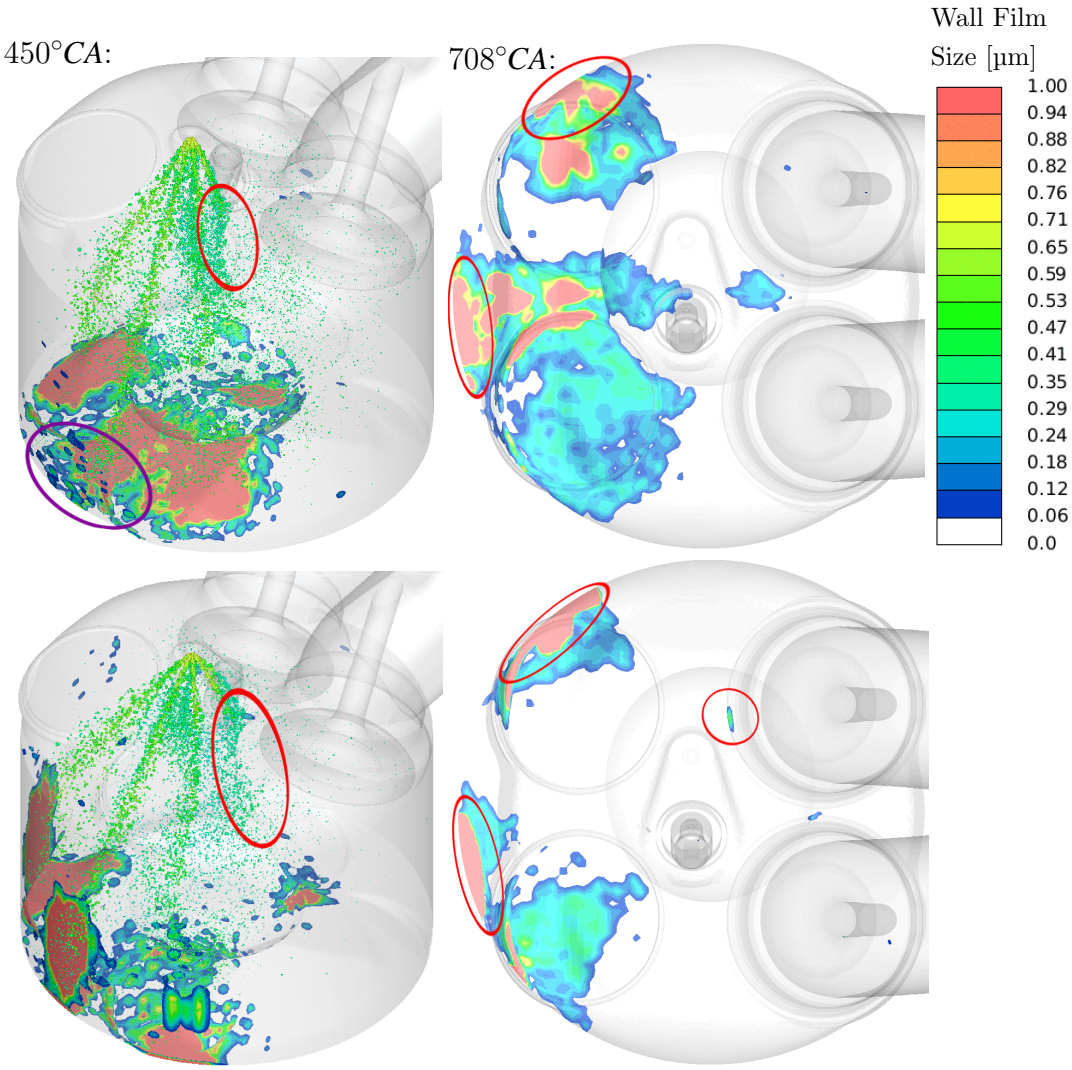

Figure 5.6: Spray formation, top: Variant 1, bottom: Variant 2.

combustion is probable, see Zahdeh et al. [2].
If accumulations are located in the piston crevice, the vaporisation ability is impaired. Due to the lowered viscosity of the oil-fuel mixture, droplets might probably strip off these accumulations, causing LSPI. Moreover, high local concentrations of wall-film on the piston crown tend to burn incomplete, leaving particulates. These particles, if not rinsed out, heat up during the next cycles causing pre-ignition series, if LSPI is initiated once, see Heiß et al.[10].
Within the CFD framework, special attention has to be paid to locations where extended wall-film accumulations are located either at the piston crown, at the cylinder liner or at the piston crevice.

Figure 5.6 presents the spray and wall-film formation structure at 450°CA

and at 708°CA right before TDC in top view. At 450°CA, the specific characteristics of the different spray axes orientations become visible. In the left row, the red marked regions in both variants highlight that the intake flow interferes with the spray cones and they get deflected towards the area below the exhaust valves. This is a common effect under high load operating conditions and results in concentrated wall wetting in these sections, see also Holly [33]. A more detailed view on the deflected spray, is provided at 426°*CA* in Figure 5.7.

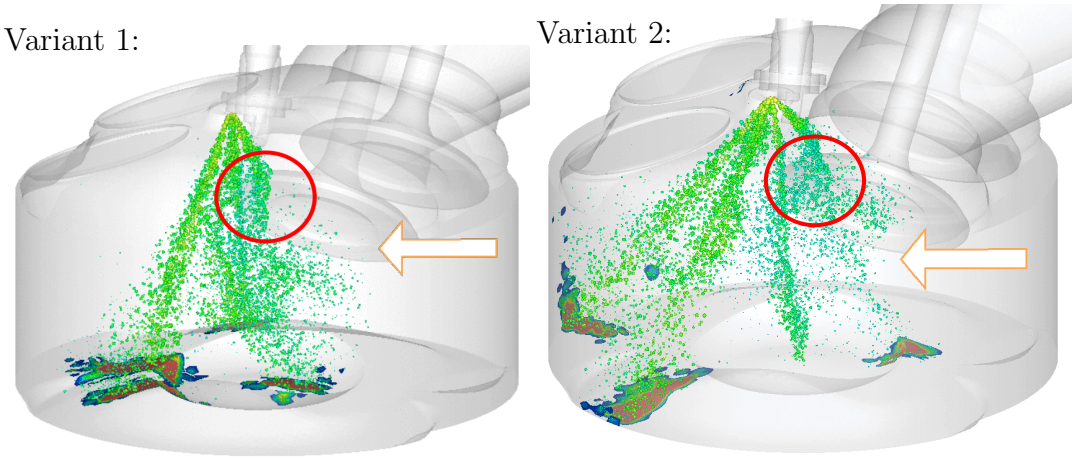

Figure 5.7: Comparison of the simulated spray deflection at 426°*CA*.

By use of an optical access, high-speed investigations of the combustion chamber are carried out at the *Institute for Powertrains and Automotive Technology*, see Figure 5.8. Within these observations, the injector according to Variant 1 is installed. The picture on the left hand side represents a view into the combustion chamber onto its components. At the right hand side, test-bench observations confirmed the finding that the spray gets deflected by the intake flow.

Another effect, visible in Figure 5.6 left, is the difference between the wetted parts. Even though the drops are deflected, target the steep orientated axes in Variant 1 mainly onto the piston crown. This is different however, in Variant 2. Intensified by the intake flow, the drops target on the cylinder liner, resulting in extended wall wetting at several locations. This is a critical effect concerning the pre-ignition tendency of that injector type.

Different spray pattern lead to different footprints of the film on the wall, which during compression result in film accumulations in the piston crevice. The wall-film structures at ignition timing are visible in Figure 5.6 at 708°CA.

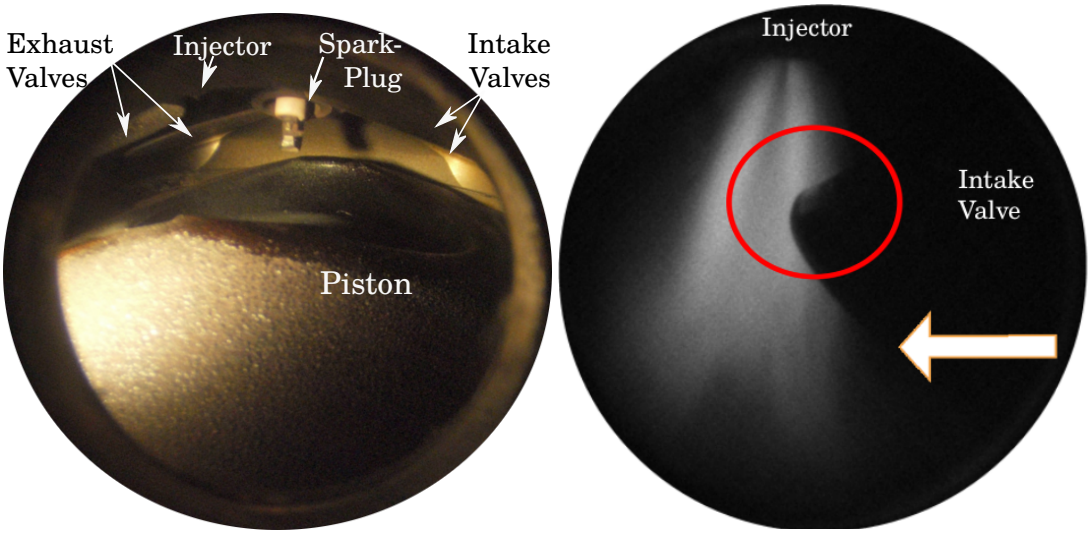

Figure 5.8: Test-bench observations, left: view into the cylinder, right: view on the deflected spray.

Large puddles of liquid film are located at the surface of the piston crown in Variant 1. The bulk of wall-film is going to vaporise and burn during power stroke, but if these pools are too thick, the remains might burn incomplete, thus increasing soot and particulate emission.
Moreover, the marked areas highlight film accumulations in the piston crevice. These accumulations develop as the liner is wetted, when the piston leaves the spray's target (already visible at 450°CA highlighted in purple). At these locations, droplets might strip off causing pre-ignitions. In Variant 2 only small pools of liquid film structures remain, but thick accumulations located in the piston crevice are visible. These are created as the piston ring gathers wall-film remains, located at the cylinder liner, see Figure 5.6 on the left hand side.

Diagram 5.3 shows the evolution of wetted film mass per wetted area, located at the piston and the cylinder liner. In Variant 1 the dominating amount of liquid film is located at the piston crown, but also at the liner a liquid film structure is evident. At about 600°CA, these film areas are gathered by the piston ring and the film mass at the liner drops to zero. Liquid film vaporisation at the piston crown continues. Thinner film structures vaporise at about 700°CA however, the trace increases as the remaining film masses covers smaller areas.
Variant 2 in contrast has the higher proportion of liquid film located at the cylinder liner. These film structures are then successively gathered by the

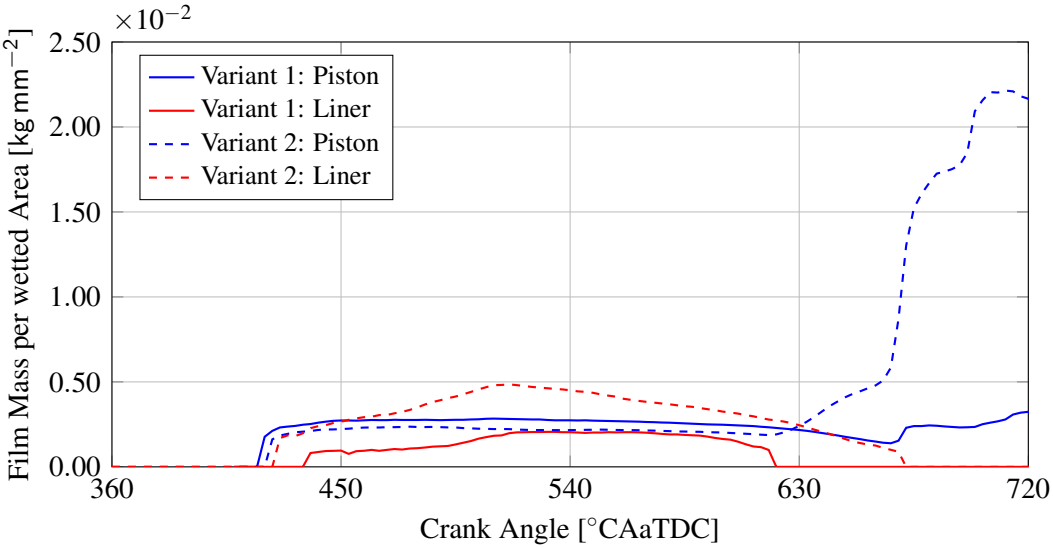

Diagram 5.3: Evolution of Liquid film mass per wetted area.

piston ring. The massive increase in the piston trace of Variant 2 clarifies how the liquid film mass accumulates on a small area close to the piston crevice. Diagram 5.3 supports the previous findings, that in Variant 2 the liner gets considerably wetted causing massive fuel accumulations at the piston, hence increasing the probability of drop stripping.

It should be noted that in Variant 2 an additional wall-film pool occurs at an intake valve, highlighted in Figure 5.6 at 708°CA. Simulation results in Figure 5.7 show that the spray is wetting the valve during intake. This is also the case in Variant 1, but since the spray does not hit the valve as intense as in Variant 2, the fuel can vaporise completely until valve closing. Valve wetting decreases the heat transfer and can cause deposits on the valve seat. Moreover, and even worse, due to the permanent shock cooling thermal induced tension on the material is increased, which can lead to crack formation.
In any case, this circumstance should be avoided, since this reduces the valves lifetime. However, it is left to mention that test-bench observation cannot confirm that the valve is wetted, since the intake valve itself blocks the view.

5.3.1 Vaporisation and Liquid Film Formation

In order to evaluate the differences in mixture preparation, the fractions of vaporised and liquid fuel during intake and compression stroke will be investi-

gated in more detail. A high vaporisation rate ensures homogeneous mixture preparation, which enhances combustion stability and lowers the pre-ignition tendency as less liquid fuel remains.

First, the differences in vaporisation rate as well as the differences in liquid fuel fractions are reviewed, see Diagram 5.4. At the start of injection (SOI) the total injected mass fraction (black) and the droplet mass fraction (red) overlap, since at the beginning only drops exist. These droplets immediately start vaporising, and with increasing vapour fraction (blue) the drop mass fractions of Variant 1 and 2 deviate from each other. Differences in the drop mass fraction correspond to the drop penetration until impingement. For Variant 1 the penetration distance is limited by the piston position. As the piston is moving down, this distance increases and therefore also the droplet lifetime increases in relation to Variant 2.

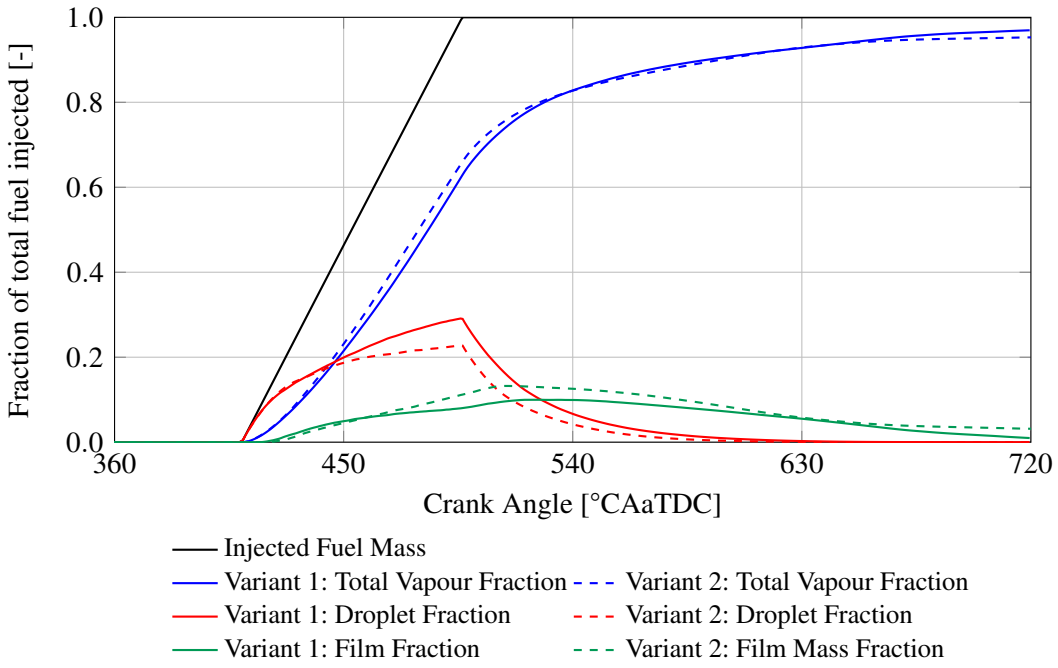

Diagram 5.4: Total vapour fraction and vapour fraction of droplet and liquid film (LF) over degree crank angle.

A little delayed to drop mass, also the liquid film (LF) mass (green) increases. Because of the more direct targeting towards the liner, more intense liquid film formation takes place in Variant 2. More details appear when reviewing Diagram 5.6. In correlation with the end of injection (EOI), a rapid decrease in the drop fraction as well as in vaporisation rate occurs.

Additional vapour is only released by liquid film structures. As in Variant 1, the film structures on the piston crown maintain their surface more extended vaporisation can take place. In Variant 2, the liquid film at the liner is collected by the piston. Since only a small liquid-gas interface remains when the liquid is trapped within the piston crevice, vaporisation almost stops.

By splitting the total vapour fraction into its original components, additional information about the impact of the spray pattern can be collected. In Diagram 5.5 the total vapour fraction is depicted in blue. It is composed of the sum of vapour fraction released by drops (red), and the vapour fraction, which is released due to liquid film vaporisation (light green). Pictured in dark green is the sum of liquid film and its corresponding vapour fraction.

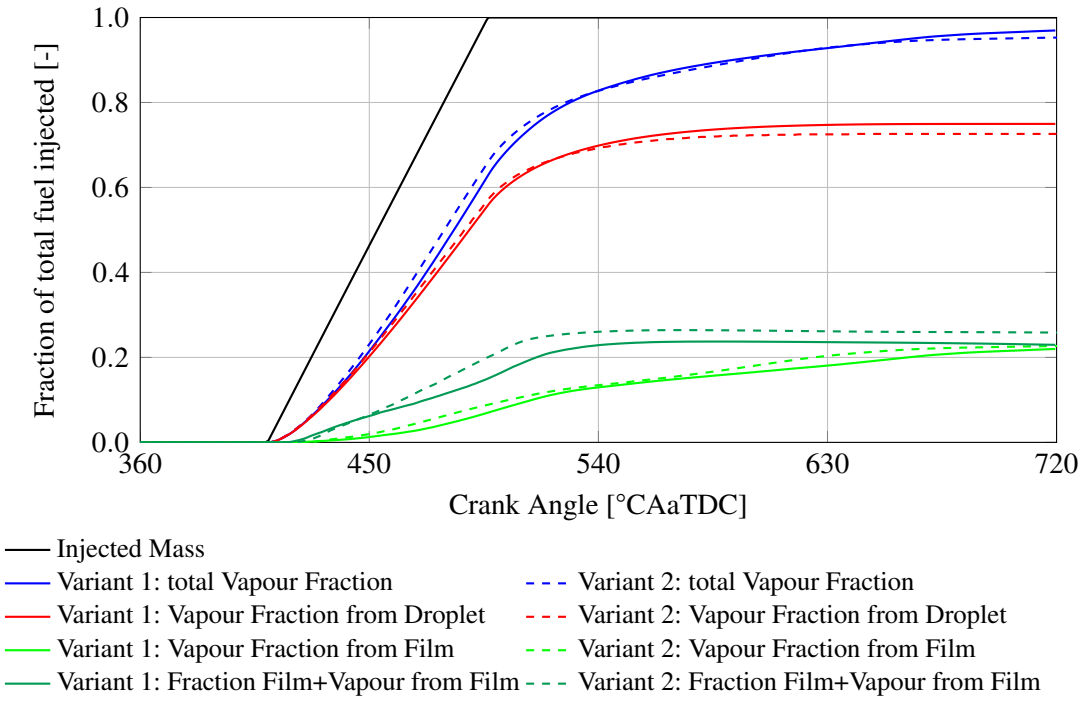

Diagram 5.5: Total vapour fraction composed of droplet vapour fraction and liquid film vapour fraction over degree crank angle.

The total vapour fraction, agrees well in both variants. During intake, vaporisation of Variant 2 is a little higher, while at the end of compression Variant 1 has finally the higher vapour fraction. During injection the majority of total vapour fraction is originating in drop vaporisation, visible by the rapid increase of these curves with almost the same rate. However, the vapour fraction due to liquid film vaporisation is getting constantly higher throughout the whole

compression phase.
At TDC almost a quarter of the total vapour fraction is originating in liquid film vaporisation. While for Variant 1 the fraction of liquid film vaporisation, the sum of liquid film fraction, and vapour from liquid film fraction align until TDC. Only a small difference remains for Variant 2. This means that almost all wall-film structures in Variant 1 can vaporise until TDC, while in Variant 2 some film fractions remain in liquid phase.

Evolution of liquid film mass is depicted in detail in Diagram 5.6. In Variant 2, the liquid film mass increases almost linearly, as the spray axes target mainly onto the cylinder liner. After the end of injection (EOI), no drops can feed the pools any more and the film mass decreases successively.

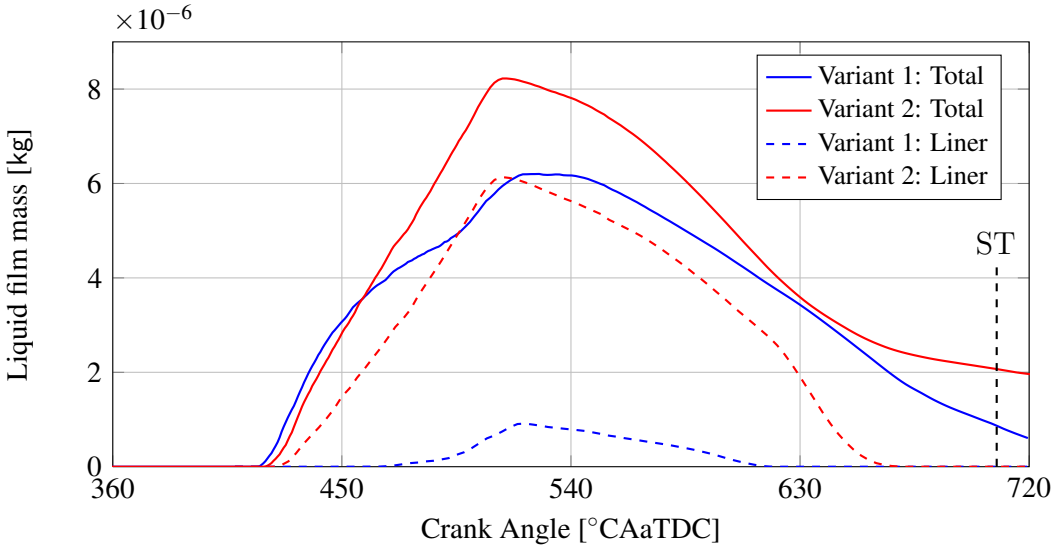

Diagram 5.6: Liquid film mass over degree crank angle.

However, the film mass evolution in Variant 1 is different. The mass increase correlates with the spray axes orientation and the piston position. At first, drops impinge primarily on the piston crown and liquid film mass increases also linearly. With sinking piston position, the piston leaves the spray's target and drops start to impinge also on the liner. This is also visible by the dashed wall-film mass trace of the liner, (see also purple marked region in Figure 5.6). Therefore, the stagnation in the film increase appear, as liquid film pools shift successively towards the cylinder liner where film mass increases again until the end of injection (EOI).

The liquid film temperature at the piston and the cylinder liner are depicted in Diagram 5.7. In Variant 1 the film temperature at the piston remains constantly at the surface temperature. However, some temperature oscillations are visible at the liner. These oscillations occur due to the immediate evaporation of small film pools as the spray successively targets onto the liner.
The temperature in Variant 2 shows no such oscillations, since the wall-films are to big for complete evaporation. The film temperature located at the liner has lower temperature than the piston. When the piston collects the liquid film of the liner wall, the films mix. Since, in Variant 2, the majority of liquid films are located at the cylinder liner the piston's film temperature decreases when the films mix.

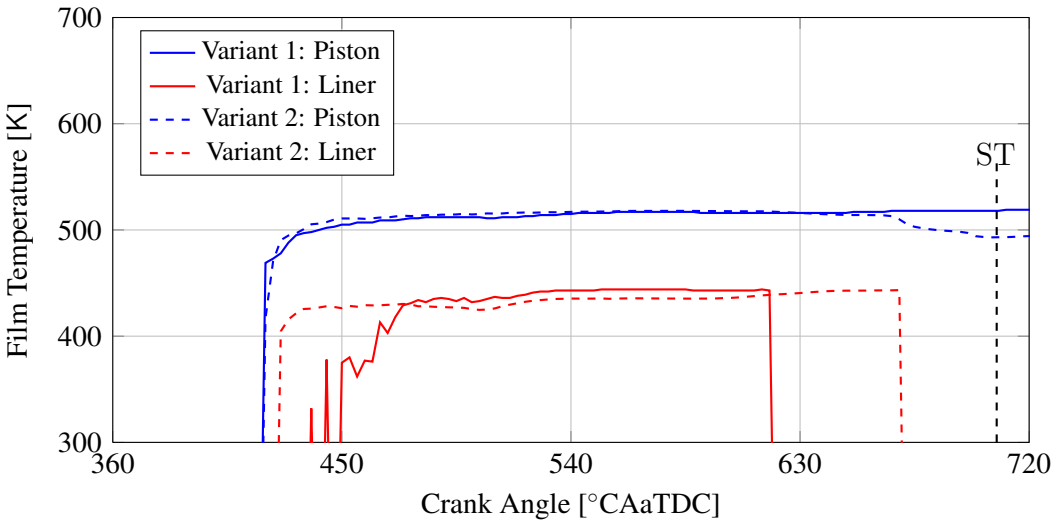

Diagram 5.7: Liquid film temperature at the piston and the cylinder liner.

Figure 5.9 presents high speed images of the combustion process. The marked spots highlight locations where pool fires occur at the piston crown. This happens, because the regular flame propagates towards the piston and ignites the thick wall-film pools located at the crown. Test bench measurements were carried out with the injector of Variant 1. The left picture shows its associated simulation results.
The existence of wall-film structures during power stroke is probable, since at TDC wall-films are visible in Diagram 5.3 as well as in Diagram 5.6. Test-bench observations confirm these CFD results, since excessive wall wetting at similar positions as the pool fires appear.
However, the CFD simulations cannot confirm any liquid film pool at the

cylinder dome between the exhaust valves. The observed spot, marked with a red arrow, might be initiated by an irregular release of droplet or a leakage of the injector. It should be mentioned, that no pre-ignitions initiated by drop stripping were observed at the test-bench. This might be reasoned in the low engine speed, at which the boost pressure was not high enough.

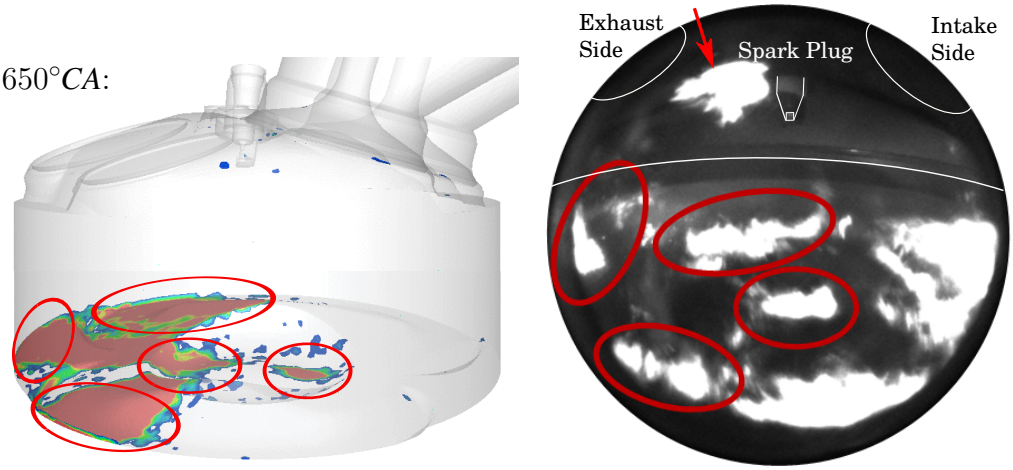

Figure 5.9: Test-bench observations of the combustion process in comparison to the wetted film areas of Variant 1.

Spark timing takes place at ∼707.25°CA, where still a considerable amount of liquid fuel is left or trapped within the piston crevice. These accumulations are transported by the piston and oil-fuel mixing is enhanced. Both injection types have in common that drop stripping is likely to occur causing pre-ignitions. But since for Variant 2 a distinct higher mass is trapped within the piston crevice, pre-ignitions are more likely to occur for this injector type.

5.3.2 Lambda Distribution

Early injection during the intake stroke is required in full load operating condition to ensure that enough time for the homogenisation of the air-fuel mixture is available.

However, with increasing engine speed, timing is reduced resulting in mixture inhomogeneities. As such inhomogeneities affect combustion stability, the air-fuel mixture distribution at spark timing is of great interest.

The spatial distribution of lambda inside the combustion chamber is depicted in Figure 5.10. Several iso-surfaces, which correspond to specific lambda values are visible and their transport due to charge motion is plotted. The first

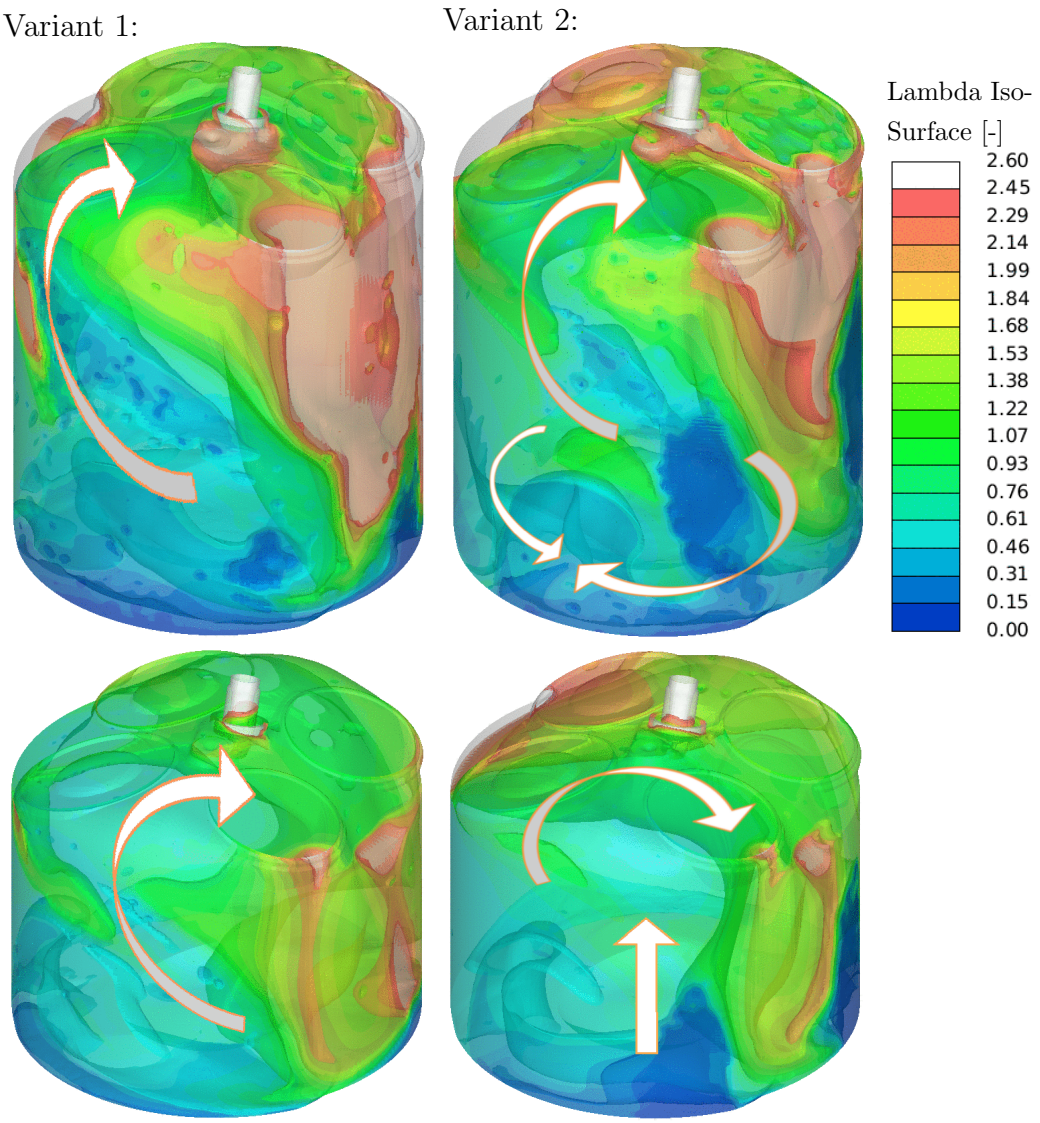

Figure 5.10: Iso-Surfaces indicating the lambda distribution, top: 580°CAaTDC, bottom: 630°CAaTDC.

row presents the mixture cloud at 580°CAaTDC and in the second row at 630°CAaTDC. The main flow structures in the figure are indicated with arrows, in order to highlight the specific movements. Successive mixing of air and fuel vapour becomes visible, revealing also the impact of the tumble motion.

It has been shown in Section 5.2, that in Variant 2 the intake flow initially accelerates a wider region of the cylinder charge. However, as the piston enters BDC, two counter turning vortices develop, see Figure 5.5. When observing the 3-dimensional evolution of the mixture cloud in Figure 5.10, the same

colliding structures can be observed. This has the effect that the rich areas at the exhaust side are separated by these counter rotating vortices. Rich mixture is trapped within this vortex and therefore, turbulent transport and mixing is slowing down, decreasing mixture homogenisation during compression.

In Figure 5.11 are section views depicted, representing the lambda distribution at ignition timing. These views reveal significant differences between the injector types. For Variant 1, a good homogenisation of the mixture especially around the spark plug is visible. Due to charge motion, the richer mixture is constantly transported away from the wall-film structures. Therefore, a lambda gradient exists from the exhaust to the intake side of the cylinder.

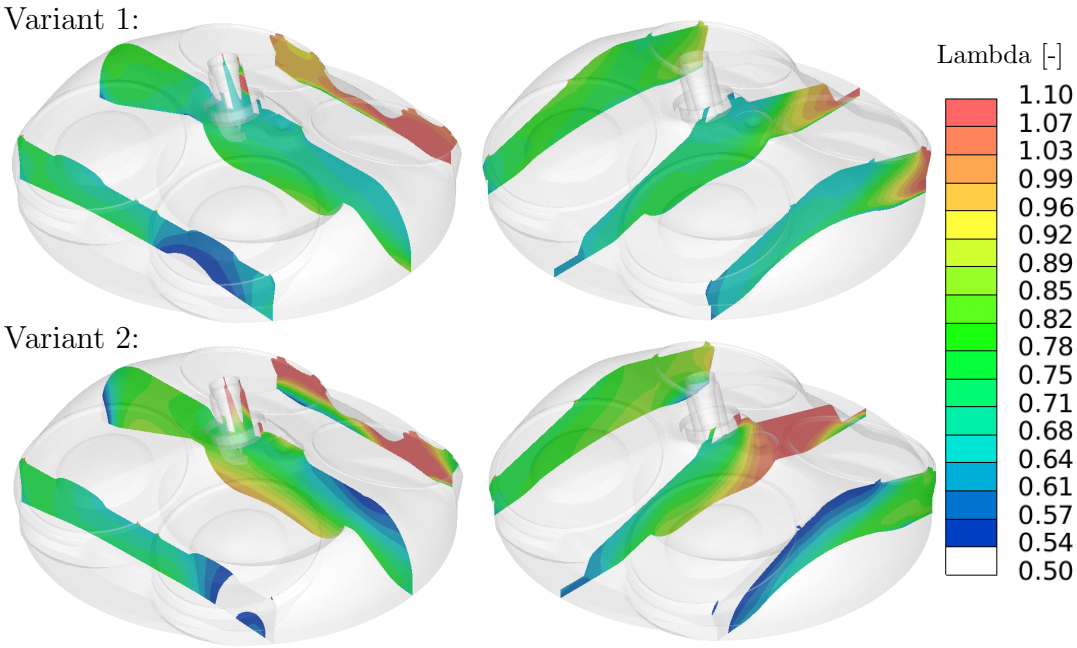

Figure 5.11: Lambda distribution at spark timing left: sections normal to the x-axes, right: sections normal to the y-axes.

In Variant 2, in contrast, mixture preparation is not sufficient homogenised, due to the unfavourable flow conditions explained in the previous paragraph. Large areas with lean mixture are located beneath the exhaust valves and even beneath the spark plug. This can cause spark misfire and the creation of unfavourable condition for the subsequent flame propagation. Correspondingly, also areas with rich mixture are present. These areas are located at the cylinder dome below the intake valves, respectively between the intake and exhaust valves.

Due to inconvenient vaporisation, lambda can deviate locally significantly from the global value. A detailed view on the lambda probability function within the combustion chamber is of interest, see Diagram 5.8. Both variants have the majority of mixture prepared close to the global lambda of 0.8, but the mixture distribution in Variant 2 is distinctly wider. Indicating, as shown in Figure 5.11, the existence of rich areas accompanied with areas of lean mixture within the chamber. This happens at the cost of well mixed areas, since they occur less frequent. However, the lambda distribution in Variant 1 is different.

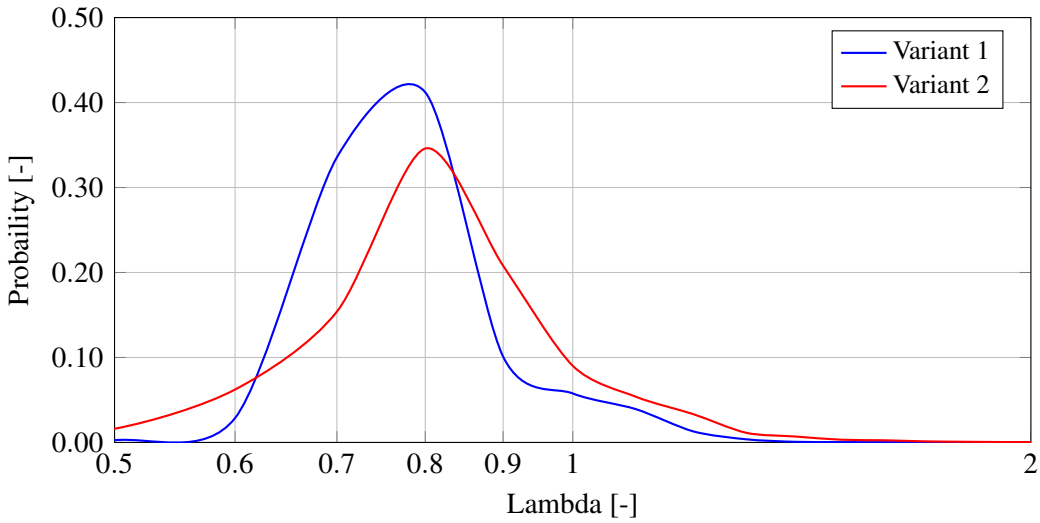

Diagram 5.8: Lambda frequency distribution at 711°CA.

Its distribution is narrower and the vast majority of air-fuel mixture is located within a range about ±0.2 around the prevailing peak. Therefore, a good homogenisation of the mixture is achieved and only small sections with lean mixture exist.

However, for stable flame propagation the local mixture surrounding the spark-plug should be distributed within the ignitable lambda range of ∼0.7 and ∼1.3, see Basshuysen [34]. In order to assess ignition stability between the different injector types, the global lambda within the cylinder and the local lambda value within a spherical volume of 5 mm radius around the spark plug are plotted in Diagram 5.9. One can see that the global lambda value is developing similarly for both injector types. However, differences arise when reviewing the trace within the local volume around the spark plug. At ignition timing the local lambda of Variant 1 is already within the ignitable range for a certain period of time. Variant 2 in contrast has a rather lean mixture distributed around the

spark plug, and stable ignition can only take place shortly before regular spark timing.

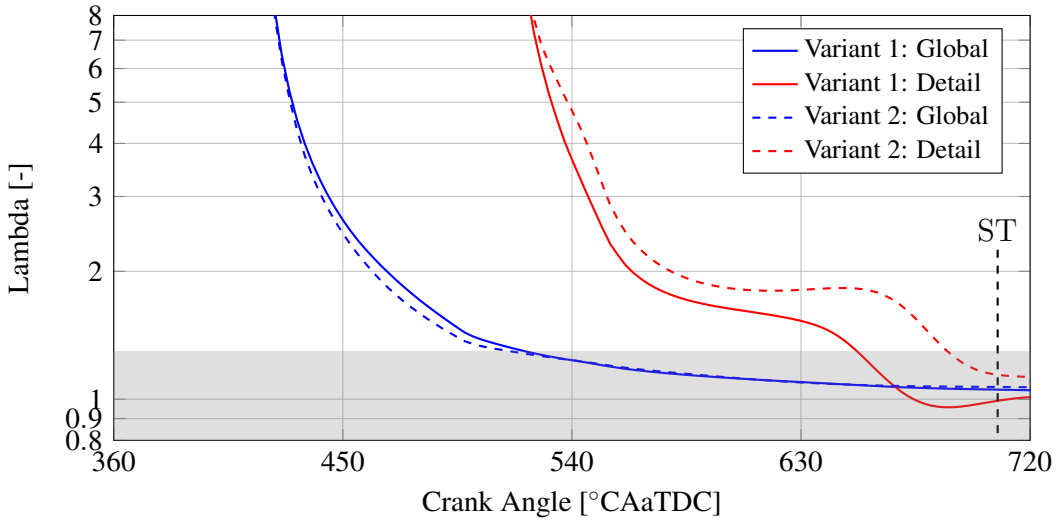

Diagram 5.9: Global lambda, and detailed lambda around spark-plug as well as spark timing (ST). Ignitable lambda region depicted in gray.

Dependent on the mixture state, the temperature within the chamber varies. As the vaporisation process takes up energy as latent heat of vaporisation, the charge is cooling down. Therefore, the leaner the mixture, the higher the temperature gets, which is evident in Diagram 5.10. According to Zahdeh [2], enrichment can help preventing pre-ignitions, because of the lower end of compression temperatures.

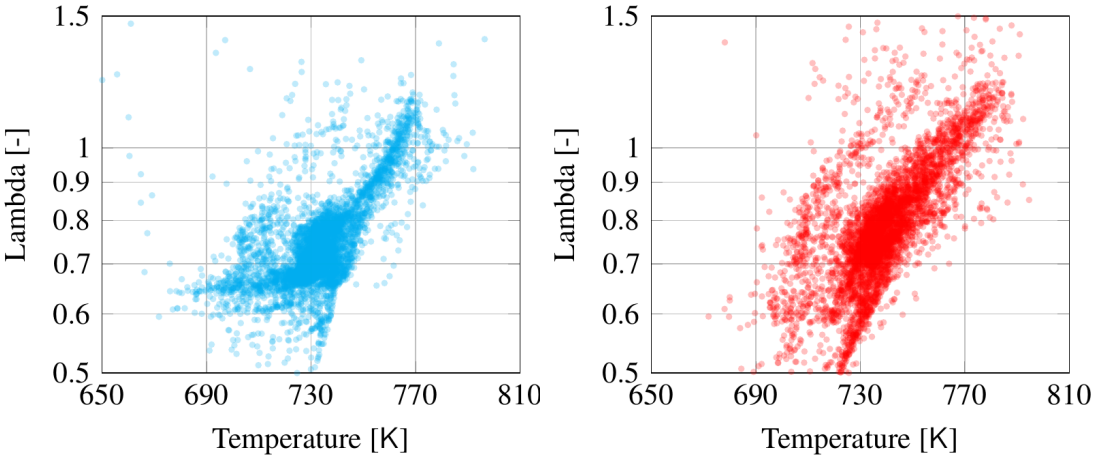

Diagram 5.10: Lambda, against Temperature at spark timing, left: Variant 1, right: Variant 2.

A lower end-of compression temperature not only suppresses self-ignition of oil vapour within the chamber, also the components wall and coolant temperature remain lower.
However, as Yasueda [5] reported, a richer mixture allows for a more rapid flame propagation with higher peak firing pressure. Therefore, severity of abnormal combustion increases the richer the mixture gets. Nevertheless, self-ignition of the fuel takes place at higher temperatures (∼1050K, Zahdeh [2]). Therefore, an agent has to exist in order to auto-ignite the mixture.
Both injector variants show tendencies to mix with lubrication oil, since both sprays are targeting the cylinder liner. But as in Variant 2 the spray instantaneously hits on the cylinder liner, oil droplets might get carried away by the impinging fuel, entering the combustion chamber. These oil drops start vaporising and since in Variant 2 several regions with higher temperature exist at spark timing, auto-ignition is likely to take place.

6 Summary and Conclusion

The previous discussions have shown, that spray formation and vaporisation as well as the wall-film formation rate depend strongly on the initialized drop size distribution. A careful coordination and validation of the impingement and wall-film model, as well as a validation of the numerical spray model against measurement data is intrinsic, in particular if pre-ignition tendencies are of interest.

In the first part, the theoretical background on spray modelling is provided and in the subsequent chapter investigated. *Star-CD*s provided atomization models for primary as well as for secondary break-up were applied and iteratively validated against measurement data. In addition to appropriate boundary condition assignment, necessitate these models tuning work, in order to meet the measurement data. Although the primary break-up model was able to meet the overall mean drop size evolution, the drop size distribution at a specific point in time is far from realistic. In agreement with the findings in Malaguti [31], the primary break-up model produces too small drop sizes at the measuring position. Hence, secondary break-up had to be skipped in order to gain realistic drop sizes.

The pursued strategy, which finally agreed well with measurements, is to manually initialise a measured drop size distribution at the nozzle exit, while considering only secondary break-up. However, this drop size distribution had to be adapted in order to meet the right drop sizes at the measuring position within the flow field, 30 mm below the nozzle. The final spray morphology as well as the sprays characteristic parameter are in good agreement with measurement data and the simulation set-up finally passed the validation process.

By use of this validated spray settings, numerical simulations of the flow field within a combustion engine, during intake and compression stroke, are performed. Two model variants, differing only in their injector axes orientation, are set-up and examined in detail.

It has been shown that dependent on the relative orientation of the intake flow and the injector axes, drops can have an amplifying or dissipating impact. Therefore, the whole flow structure propagates different, which is reasoned in the differences in momentum exchange.
While the steep into the cylinder orientated spray axes of Variant 1 channel the intake flow creating an uniform tumble vortex along the whole cylinder height, the charge motion of Variant 2 behaves differently. The shallow spray orientation causes the intake flow to spread out. Therefore, in addition to the general tumble motion a small vortex develops at the cylinder bottom, increasing dissipation. Within this vortex, momentum, energy, and mass is transported in isolation of the surrounding charge. This circumstance contributes to the mixture inhomogeneities at spark timing.

Both, simulation results as well as test-bench observations show a deflection of the spray towards the cylinder half of the exhaust valves. Therefore, fuel accumulations on the liner, the piston crown, as well as in the piston crevice are located below the exhaust valves.
Dahnz et al. [3] as well as Zahdeh et al. [2] already reported the increase of pre-ignition tendency, if the spray is targeting onto the liner. Moreover, the previous investigations revealed that this is not only caused by the higher wall-film portions alone, but also by the inconvenient effects, which cause mixture inhomogeneities supporting pre-ignition tendency.
Wall-film structures located at the piston crown tend to burn incomplete, leaving deposits, which if not rinsed out tend to cause subsequent pre-ignitions if a pre-ignition series has already been started. However, fuel-oil mixture droplets, stripping off film accumulations originally cause pre-ignitions. Within the previous investigations, special attention is paid to such accumulations and their specific parameters. In general, it can be stated that the more the cylinder liner is wetted, the thicker the fuel accumulations within the piston crevice become. Therefore, the higher the risk for pre-ignition tendency gets.

It has been shown that both injector variants provide tendencies for pre-ignition initiation. Hence, in accordance with literature, Variant 2 shows the higher tendency for pre-ignitions.
Variant 1 provides several advantages, which can be summarised as follows. Because of the spray axes orientation liner wetting is reduced to a minimum.

Hence, film accumulations within the piston crevice can be avoided to a certain extent. Therefore, also mixing with lubrication oil is avoided, since the wall-film formation primarily takes place at the piston crown. Residual liquid film pools maintain a relatively big area, which enhances film vaporisation. Another positive, although small effect is that this spray pattern enhances charge motion. Maintaining the intake flows kinetic energy improves flame propagation, which again has a positive effect on pre-ignition tendencies in subsequent cycles.
Because of these reasons, Variant 1 is superior and further measures incorporating the pre-ignition tendencies of this engine should apply for this injector type.

Nevertheless, there is room for improvements. Since primary break-up is skipped, the pursued injection strategy is not in general applicable, because the relationship between injection parameter and spray characteristics is lost. In order to take the full spectrum of spray formation into account, additional investigations should be conducted. Further investigations on the primary break-up model set-up should be incorporated to take also the flow conditions at the nozzle exit into account. In addition, secondary break-up is important to properly regard droplet disintegration due to aerodynamic forces.
Only by applying both primary and secondary break-up models the whole spray formation process can be determined properly.

A more detailed assessment of combustion stability and energy efficiency could be obtained by extending the numerical simulations via incorporating reaction kinetics and combustion models.
Additional investigations under different engine speeds might allow for a larger picture on the whole engine performance.
It needs to be pointed out that within the previous investigations only one intake and compression stroke has been considered. However, film structures within the piston crevice must have to add up within the next cycles. Therefore, it has to be expected that the liquid film mass will increase further, which increases the pre-ignition tendency.

Within the scope of more detailed investigations the liner surface, which is wetted with lubrication oil, should be modelled in more detail. Currently the liner is modelled as a dry wall, if also the lubrication oil is considered, a more

accurate description of droplet impingement on the liquid-liquid interface, as well as of the oil-fuel mixing process would improve the simulation results. Moreover, critical areas within the piston crevice are not modelled in detail because of the high differences in dimensions. However, a detailed model of the piston crevice area as well as on the drop stripping process would provide rich information on the pre-ignition initiation process.

Bibliography

[1] U. Tietge and P. Mock, "CO2 emissions from new passenger cars in the EU: Car manufacturers' performance in 2013," *The ICCT*, June 2014. Available: 12.12.2014.

[2] A. Zahdeh, P. Rothenberger, W. Nguyen, M. Anbarasu, S. Schmuck-Soldan, J. Schaefer, and T. Goebel, "Fundamental approach to investigate pre-ignition in boosted SI engines," tech. rep., SAE Technical Paper, 2011.

[3] C. Dahnz and U. Spicher, "Irregular combustion in supercharged spark ignition engines - pre-ignition and other phenomena," *International Jounal of Engine Research*, vol. 11, 12 2010.

[4] M. Heiss and T. Lauer, "Simulation of the Mixture Preparation for an SI Engine using Multi-Component Fuels," in *STAR global conference*, 2012.

[5] S. Yasueda, K. Takasaki, and H. Tajima, "The Abnormal Combustion caused by Lubricating oil on High MEP Gas Engines," in *13. Tagung "Der Arbeitsprozess des Verbrennungsmotors"*, Sept. 2011.

[6] G. P. Merker, C. Schwarz, and R. Teichmann, *Grundlagen Verbrennungsmotoren.* Praxis. ATZ/MTZ-Fachbuch, Vieweg+Teubner Verlag / Springer Fachmedien Wiesbaden GmbH, Wiesbaden, 2011.

[7] G. Merker, C. Schwarz, G. Stiesch, and F. Otto, *Verbrennungsmotoren.: Simulation der Verbrennung und Schadstoffbildung.* Lehrbuch : Maschinenbau, Teubner B.G. GmbH, 2004.

[8] R. Van Basshuysen, *Ottomotor mit Direkteinspritzung: Verfahren, Systeme, Entwicklung, Potenzial.* Atz/Mtz-Fachbuch, Springer Fachmedien Wiesbaden, 2013.

[9] C. Dahnz, K.-M. Han, and M. Magar, "Untersuchung des Auftretens und der Ursache von Selbstzündungen vor Zündungseinleitung bei aufgeladenen Motoren mit hohem Verdichtungsverhältnis," tech. rep., Institut für Kolbenmschinen, 2010.

[10] M. Heiß, T. Lauer, N. Bobicic, and S. Pritze, "Modellansatz zur Entstehung von Vorentflammungen," *MTZ- Motortechnische Zeitschrift*, vol. 01/2014, pp. 64–71, 2014.

[11] D.-I. J.-M. Zaccardi, I. M. Lecompte, I. L. Duval, and D.-I. A. Pagot, "Vorentflammung an hoch aufgeladenen Ottomotoren," *MTZ-Motortechnische Zeitschrift*, vol. 70, no. 12, pp. 938–945, 2009.

[12] P. Stefan, K. Heiko, M. Max, and S. Robert, "Untersuchung des Auftretens und der Ursache von Selbstzündungen vor Zündungseinleitung bei aufgeladenen Motoren mit hohem Verdichtungsverhältnis," in *Informationstagung Motoren, Herbst 2012,Dortmund*, 2012.

[13] K. Takeuchi, K. Fujimoto, S. Hirano, and M. Yamashita, "Investigation of Engine Oil Effect on Abnormal Combustion in Turbocharged Direct Injection - Spark Ignition Engines," *SAE Technical Paper*, vol. 01, 10 2012.

[14] J. Heywood, *Internal combustion engine fundamentals*. McGraw-Hill series in mechanical engineering, McGraw-Hill, 1988.

[15] C. Baumgarten, *Mixture Formation in Internal Combustion Engines*. Heat and Mass Transfer, Springer, 2006.

[16] N. Ashgriz, *Handbook of Atomization and Sprays: Theory and Applications*. SpringerLink : Bücher, Springer, 2011.

[17] A. Wierzba, "Deformation and breakup of liquid drops in a gas stream at nearly critical Weber numbers," *Experiments in Fluids*, vol. 9, no. 1-2, pp. 59–64, 1990.

[18] CD-adapco, *STAR-CD Methodology Version 4.18*. CD-adapco, 2012.

[19] J. J. Batteh and E. W. Curtis, "Modeling transient fuel effects with alternative fuels," tech. rep., SAE Technical Paper, 2005.

[20] T. Waba, "Entwicklung und Bewertung eines Mehrkomponenten-Kraftstoffmodells zur numerischen Simulation der Gemischaufbereitung von ROZ 95, Ethanol und E85," Master's thesis, Technische Universität Wien, April 2011.

[21] A. A. Amsden, P. Orourke, and T. Butler, "KIVA-2: A computer program for chemically reactive flows with sprays," *NASA STI/recon technical report N*, vol. 89, p. 27975, 1989.

[22] S. Pope, *Turbulent Flows*. Cambridge University Press, 2000.

[23] J. H. Ferziger and M. Peric, *Numerische Strömungsmechanik*. Springer London, Limited, 2008.

[24] F. Williams, *Combustion Theory: The Fundamental Theory of Chemically Reacting Flow Systems*. Combustion science and engineering series, Perseus Books Group, 1985.

[25] I. Glassman, *Combustion*. Elsevier Science, 1997.

[26] B. Abramzon and W. Sirignano, "Droplet vaporization model for spray combustion calculations," *Int. J Heat Mass Transfer*, vol. 32, no. 9, pp. 1605–1618, 1989.

[27] "Pool Boiling Regimes." https://www.thermalfluidscentral.org/encyclopedia/images/d/dd/Boiling_j_%284%29.jpg. Available: 07.10.2014.

[28] C. Bai and A. Gosman, "Development of methodology for spray impingement simulation," tech. rep., SAE Technical Paper, 1995.

[29] D. Torres, P. O'rourke, and A. Amsden, "Efficient multicomponent fuel algorithm," *Combustion Theory and Modelling*, vol. 7, no. 1, pp. 67–86, 2003.

[30] M. Panão and A. Moreira, "Thermo-and fluid dynamics characterization of spray cooling with pulsed sprays," *Experimental Thermal and Fluid Science*, vol. 30, no. 2, pp. 79–96, 2005.

[31] M. S., F. S., and C. G., "Numerical characterization of a new high-pressure multi-hole GDI injector," in *ILASS-Europe 2010,23rd Annual Conference on Liquid Atomization and Spray Systems*, Sept. 2010. Available: 24.11.2014.

[32] J. Lumley, *Engines: An Introduction*. Cambridge University Press, 1999.

[33] W. Holly, "Reaktionskinetische Analyse der klopfenden Verbrennung an einem aufgeladenen Ottomotor mit Direkteinspritzung," Master's thesis, Technische Universität Wien, Mai 2013.

[34] R. van Basshuysen and F. Schäfer, *Handbuch Verbrennungsmotor: Grundlagen, Komponenten, Systeme, Perspektiven*. ATZ-MTZ Fachbuch, Vieweg + Teubner, 2010.